Laboratory measurements of HDO/H2O isotopic fractionation during ice deposition in simulated cirrus clouds

Article *in* Proceedings of the National Academy of Sciences · May 2017

DOI: 10.1073/pnas.1618374114

CITATION
1

READS
63

8 authors, including:

Volker Ebert
Physikalisch-Technische Bundesanstalt
270 PUBLICATIONS **2,462** CITATIONS
SEE PROFILE

Ottmar Möhler
Karlsruhe Institute of Technology
284 PUBLICATIONS **6,180** CITATIONS
SEE PROFILE

E. J. Moyer
University of Chicago
94 PUBLICATIONS **1,437** CITATIONS
SEE PROFILE

Laboratory measurements of HDO/H_2O isotopic fractionation during ice deposition in simulated cirrus clouds

Kara D. Lamb[a,1], Benjamin W. Clouser[a], Maximilien Bolot[b,2], Laszlo Sarkozy[b], Volker Ebert[c], Harald Saathoff[d], Ottmar Möhler[d], and Elisabeth J. Moyer[b,3]

[a]Department of Physics, University of Chicago, Chicago, IL 60637; [b]Department of the Geophysical Sciences, University of Chicago, Chicago, IL 60637; [c]Physikalisch-Technische Bundesanstalt, 38116 Braunschweig, Germany; and [d]Institute for Meteorology and Climate Research, Karlsruhe Institute of Technology, 76021 Karlsruhe, Germany

Edited by Mark H. Thiemens, University of California, San Diego, La Jolla, CA, and approved April 5, 2017 (received for review November 5, 2016)

The stable isotopologues of water have been used in atmospheric and climate studies for over 50 years, because their strong temperature-dependent preferential condensation makes them useful diagnostics of the hydrological cycle. However, the degree of preferential condensation between vapor and ice has never been directly measured at temperatures below 233 K (−40 °C), conditions necessary to form cirrus clouds in the Earth's atmosphere, routinely observed in polar regions, and typical for the near-surface atmospheric layers of Mars. Models generally assume an extrapolation from the warmer experiments of Merlivat and Nief [Merlivat L, Nief G (1967) *Tellus* 19:122–127]. Nonequilibrium kinetic effects that should alter preferential partitioning have also not been well characterized experimentally. We present here direct measurements of HDO/H_2O equilibrium fractionation between vapor and ice (α_{eq}) at cirrus-relevant temperatures, using in situ spectroscopic measurements of the evolving isotopic composition of water vapor during cirrus formation experiments in a cloud chamber. We rule out the recent proposed upward modification of α_{eq}, and find values slightly lower than Merlivat and Nief. These experiments also allow us to make a quantitative validation of the kinetic modification expected to occur in supersaturated conditions in the ice–vapor system. In a subset of diffusion-limited experiments, we show that kinetic isotope effects are indeed consistent with published models, including allowing for small surface effects. These results are fundamental for inferring processes on Earth and other planets from water isotopic measurements. They also demonstrate the utility of dynamic in situ experiments for studying fractionation in geochemical systems.

isotopic fractionation | water vapor | cirrus clouds | ice deposition | diffusivity ratio

Accurate values of the vapor–ice isotopic fractionation factor are needed for many studies in paleoclimate, atmospheric science, or planetary science that use HDO/H_2O measurements as tracers: for paleotemperature or paleoaltimetry reconstructions with process-based models (1), for characterizing the hydrological cycle (2–4), for diagnosing convective transport of water to the tropical tropopause layer (TTL) (5–9), and for understanding the sources of water and the history of hydrogen escape on Mars (10, 11). In Earth's atmosphere, HDO has been measured by in situ balloon and aircraft instruments (6, 12), by nadir-sounding satellite instruments (13, 14), and by limb sounders that look at the edge of Earth's atmosphere and produce high-vertical-resolution profiles (15–17). The ExoMars mission, launched in 2016, will measure similar profiles on Mars (18). To date, water isotopologues have been introduced into at least 10 general circulation models of Earth (e.g., refs. 19–21) and one of Mars (10). The science conclusions drawn from comparing model output to isotopic measurements depend sensitively on the models' assumed value for isotopic fractionation. For the HDO/H_2O system, all use extrapolations of α_{eq} from the measurements of Merlivat and Nief (22) at temperatures warmer than the regime for cirrus formation. (We denote the expression for the temperature dependence in ref. 22 as M67.)

Measuring α_{eq} at cold temperatures is difficult largely because water vapor pressure becomes so small: in the cold uppermost troposphere, mixing ratios of H_2O can be a few parts per million, and those of HDO can be a few parts per billion. However, equilibrium fractionation becomes very large in these conditions, in part because the effect rises as $\sim 1/T^2$. The temperature dependence is typically assumed as

$$\alpha_{eq}(T) = \exp\left(a_0 + \frac{a_1}{T^2}\right), \quad [1]$$

the high-temperature limit for fractionation during gas condensation (23). Equilibrium fractionation in water is also particularly strong for deuterium substitution, because the effect scales to first order with the difference of the inverse of the isotopic masses (e.g., refs. 24 and 25).

In M67 (22), extrapolated to 190 K, α_{eq} exceeds 1.4 ($> 40\%$ HDO enhancement in ice), among the largest single-substitution

Significance

The preferential deposition of heavy water (HDO or $H_2^{18}O$) as ice is a fundamental tracer in the geosciences, used for understanding paleoclimate and water cycling, but the basic physical chemistry is not well measured. We describe here measurements of the preferential fractionation of HDO vs. H_2O at the cold temperatures relevant to cirrus clouds on Earth and snow on Mars. We also provide a quantitative demonstration of kinetic isotope effects in nonequilibrium conditions, and show how targeted dynamic experiments can be used to understand processes at ice surfaces.

Author contributions: K.D.L., M.B., and E.J.M. led the fractionation analysis; E.J.M. directed the construction and operation of ChiWIS; L.S. led the design of ChiWIS; K.D.L., B.W.C., and L.S. built and operated ChiWIS; K.D.L., B.W.C., and L.S. analyzed raw ChiWIS data to produce isotopic measurements; H.S. provided and operated multipass optics; H.S. and O.M. operated AIDA during the IsoCloud campaign; H.S. and O.M. provided and interpreted AIDA instrument data; V.E. provided SP-APicT and APeT data; and K.D.L., M.B., and E.J.M. wrote the paper.

The authors declare no conflict of interest.

This article is a PNAS Direct Submission.

Data deposition: The IsoCloud datasets and isotopic model can be found at https://publish.globus.org/jspui/handle/11466/247.

[1]Present address: Chemical Sciences Division, Earth System Research Laboratory, National Oceanic and Atmospheric Administration, Boulder, CO 80305.

[2]Present address: Program in Atmospheric and Oceanic Sciences, Princeton University, Princeton, NJ 08540.

[3]To whom correspondence should be addressed. Email: moyer@uchicago.edu.

This article contains supporting information online at www.pnas.org/lookup/suppl/doi:10.1073/pnas.1618374114/-/DCSupplemental.

vapor pressure isotope effects seen in natural systems. In 2013, Ellehøj et al. (26) reported measurements implying still stronger fractionation, with α_{eq} nearly 1.6 when extrapolated to 190 K, i.e., preferential partitioning α_{eq}-1 nearly 50% higher than implied by M67 (22). (We denote the expression for the temperature dependence in ref. 26 as E13; see *SI Appendix*, Table S1 for all previous estimates.) That difference would significantly alter interpretations of water isotopic measurements.

In many real-world conditions, kinetic effects during ice deposition can modify isotopic fractionation from the equilibrium case. Jouzel and Merlivat (27) explained nonequilibrium isotopic signatures in polar snow as the result of reduced effective fractionation when ice grows in diffusion-limited (and hence supersaturated) conditions, reasoning that preferential uptake should isotopically lighten the near-field vapor around growing ice crystals, with the effect amplified by the lower diffusivity of the heavier isotopologues. These diffusive effects are important for rain as well as snow, because most precipitation originates in mixed-phase (ice and liquid water) clouds, and can therefore alter "deuterium excess" in rainwater, a metric of nonequilibrium conditions that is often interpreted as reflecting only the initial evaporation of water (28). Despite the importance of kinetic effects during ice deposition, they are poorly characterized by experimental studies.

In the framework of Jouzel and Merlivat (27), the kinetic modification factor α_k can be written in terms of properties of the bulk gas,

$$\alpha_k = \frac{S_i}{\alpha_{eq} \cdot \mathrm{d}\,(S_i - 1) + 1}, \qquad [2]$$

where S_i is the supersaturation over ice and d (following the notation of ref. 29) is the isotopic ratio of diffusivities of water molecules in air. (That is, $\mathrm{d} = D_v/D'_v$, where D_v and D'_v are the molecular diffusivities of H_2O and HDO, respectively.) The effective isotopic fractionation is then $\alpha_{eff} = \alpha_{eq} \cdot \alpha_k$. The modification can be large at high supersaturations and cold temperatures, e.g., when ice nucleates homogeneously within aqueous sulfate aerosols in the upper troposphere ($S_i = 1.5$, T = 190 K). For ice growth occurring at these conditions, the preferential partitioning would be reduced by over 55% ($\alpha_{eq} = 1.43$, but $\alpha_{eff} = 1.24$) even conservatively using one of the lowest published estimates of d, that from Cappa et al. (ref. 30, d = 1.0164). The diffusive model of Eq. **2** is widely used but poorly validated. Kinetic effects during ice growth have been explored in three prior experimental studies (27, 31, 32). Although these provided qualitative support, relating supersaturated conditions to reduced fractionation or gradients in vapor isotopic composition, no experiments produced quantitative agreement with Eq. **2**.

Recent theoretical studies have proposed extending the diffusive model to include surface processes at the vapor–ice interface, which may become important when ice crystals are small (of order microns). In these conditions, surface impedance becomes comparable to vapor impedance, and any difference in deposition coefficients between isotopologues would contribute to kinetic isotope effects (29, 33). (The deposition coefficient quantifies the probability that a molecule incident on a growing ice crystal will be incorporated into the crystal lattice. Again following ref. 29, we define its isotopic ratio as $\mathrm{x} = \beta/\beta'$, where β and β' are the deposition coefficients for H_2O and HDO, respectively.) The deposition coefficient ratio has never been measured, but suggested plausible values of x = 0.8 to 1.2 would, in our example of upper tropospheric cirrus formation, further alter preferential partitioning by an additional 7 to 9%. Previous experimental studies of kinetic fractionation (27, 31, 32) were not sensitive to surface processes, because all involved large dendritic crystals in a regime where growth is not limited by surface effects (e.g., refs. 29, 34, and 35).

IsoCloud Campaigns

To investigate both equilibrium and kinetic isotopic effects at low temperatures, we carried out a series of experiments at the Aerosol Interactions and Dynamics in the Atmosphere (AIDA) cloud chamber during the 2012–2013 IsoCloud (Isotopic fractionation in Clouds) campaign. AIDA is a mature facility that has been widely used for studies of ice nucleation and cirrus formation (e.g., refs. 36–38). In the IsoCloud experiments, we determine isotopic fractionation not from static conditions as in previous studies but by measuring the evolving concentrations of HDO and H_2O vapor as ice forms. These experiments more closely replicate the conditions of ice formation in the atmosphere. Results reported here are derived from a new in situ tunable diode laser absorption instrument measuring HDO and H_2O (the Chicago Water Isotope Spectrometer, ChiWIS) and from AIDA instruments measuring total water, water vapor, ice crystal number density, temperature, and pressure (Fig. 1).

AIDA experiments produce rapid cooling inside the cloud chamber by pumping and adiabatic expansion, causing nucleation and growth of ice particles in situ. In a typical experiment (Fig. 2), cooling drives supersaturation above the threshold for ice nucleation within a minute of the onset of pumping. ($S_i \approx 1$ to 1.2 for heterogeneous and 1.4 to 1.6 for homogeneous nucleation.) As ice grows, the isotopic ratio of chamber water vapor lightens as the heavier isotopologues preferentially condense. For a typical cooling of 5 K to 9 K, water vapor

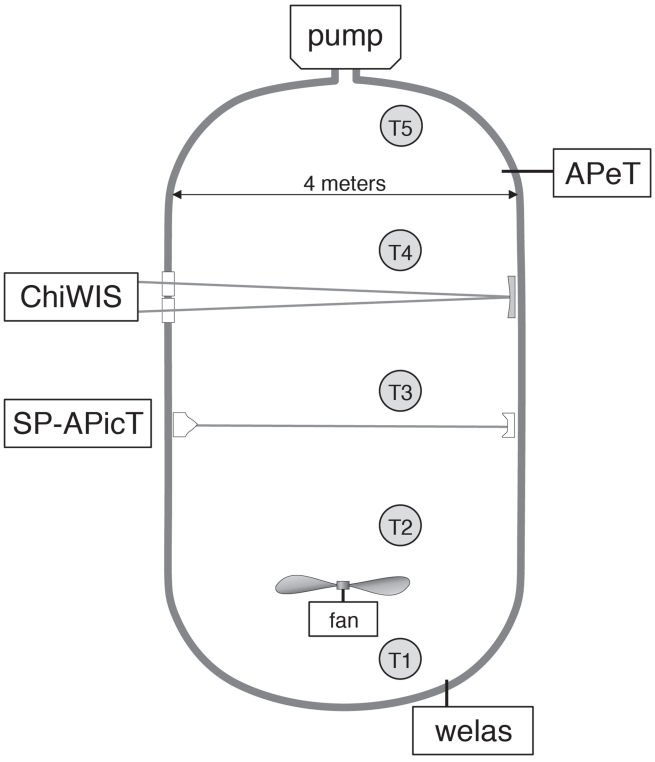

Fig. 1. Positioning of the instruments used in this analysis during the IsoCloud experiment campaigns. (Additional instruments also participated in the IsoCloud campaigns.) ChiWIS measures in situ isotopic water vapor (HDO/H_2O), SP-APicT [single-pass AIDA Physikalisch-Chemisches Institut (PCI) in cloud tunable diode laser (TDL)] measures in situ water vapor (H_2O only), and APeT (AIDA PCI extractive TDL) measures total water (H_2O ice and vapor). We take gas temperature as the average of thermocouples T1 through T4. Data from the welas optical particle counter are used to derive the effective ice particle diameter and in calculating kinetic isotope effects. SP-APicT data are used in cases of thick ice clouds to determine slight corrections for backscatter effects in ChiWIS.

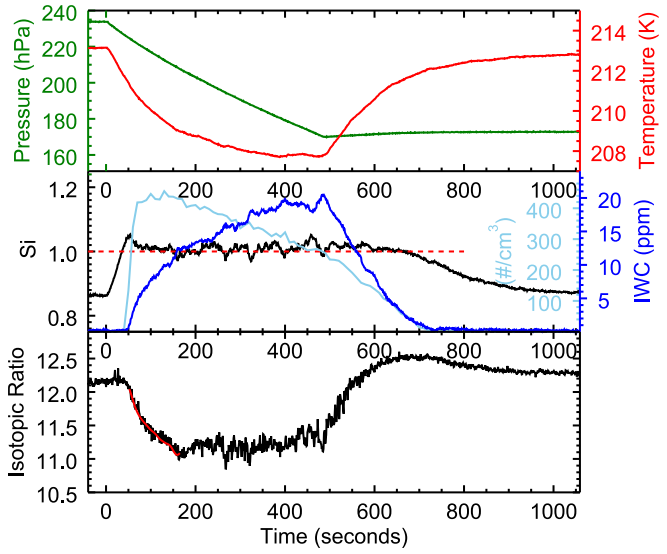

Fig. 2. Typical adiabatic expansion experiment. (*Top*) Pressure drop (green) causes drop in temperature (red) for ∼2 min before thermal flux from the wall becomes important. (*Center*) Ice formation [light blue, number density of ice particles; dark blue, total ice water content (IWC)] begins when critical supersaturation (black) is reached. (Ice water content is given in units of equivalent mixing ratio in chamber air—parts per million by volume—if ice were sublimated to the vapor phase.) (*Bottom*) Vapor isotopic ratio (black, doped to ∼12× natural abundance) shows three stages: initial decline as ice growth draws down vapor, constant period when ice growth is driven by wall flux, and final rise as ice sublimates. Fractionation factor is derived from model fit to initial period (red). After sublimation, vapor isotopic ratio exceeds starting value because of wall contribution; system then reequilibrates over ∼5 min. Fluctuations while ice is present reflect inhomogeneities due to turbulent mixing.

drops by 30 to 50% and the vapor HDO/H_2O ratio drops by ∼10%. After several minutes, the walls (prepared with a thin ice layer in initial isotopic equilibrium with vapor) become a source of both water vapor and heat (39), and vapor mixing ratio and isotopic composition stabilize even while ice growth continues. Most IsoCloud experiments reach saturation quickly after nucleation, but, in dilute conditions, ice growth can take several minutes to draw chamber vapor down to equilibrium. The resulting ambient supersaturation during ice growth depends on the nucleation threshold, growth rate, and ice particle number density.

The analysis here uses 28 experiments during the March through April 2013 IsoCloud campaign, covering a wide range of conditions: initial temperatures from 234 K to 194 K, mean supersaturation over ice (S_i) of 1.0 to 1.4, mean ice particle diameter of 2 μm to 14 μm, and ice nucleation via mineral dust, organic aerosols, and sulfate aerosols. (Temperatures are restricted to 234 K and below to preclude coexistence of liquid and ice phases, which would complicate isotopic interpretation.) Each campaign day involved four to six expansion experiments at the same initial temperature, separated by 1 h to 2 h to reestablish equilibrium. To boost signal to noise for isotopic measurements, all water introduced into AIDA was isotopically doped to produce HDO/H_2O ratios of ∼10 to 20× natural abundance (defined as VSMOW). See *SI Appendix* for further information about instruments, experiments, data treatment, and campaign. *SI Appendix*, Table S3 and Fig. S4 show conditions and results for all experiments used in this analysis.

Analysis

Interpreting cirrus formation experiments requires consideration of three factors: equilibrium fractionation, kinetic effects, and any additional sources of water. In the absence of other sources, water vapor isotopic composition would evolve by simple Rayleigh distillation, with vapor progressively depleted as ice grows and HDO is segregated into the ice phase. The effective isotopic fractionation $\alpha_{\mathrm{eff}} = \alpha_{\mathrm{eq}} \cdot \alpha_{\mathrm{k}}$ would then be the slope of that evolution (Fig. 3). Isotopic evolution deviates from Rayleigh distillation when the wall contribution becomes nonnegligible.

We account for all three effects by fitting each experiment to a model derived from mass balance over H_2O and HDO,

$$\frac{dR_v}{dt} = -(\alpha_{\mathrm{eff}} - 1)\, R_v \frac{P_{\mathrm{vi}}}{r_v} + (\gamma - 1)\, R_v \frac{S_{\mathrm{wv}}}{r_v}. \qquad [3]$$

(For further discussion, see *SI Appendix*, *Isotopic Model for Expansion Experiments*.) We measure the water vapor concentration r_v and isotopic composition $R_v = r'_v/r_v$ (where r'_v and r_v denote the mass mixing ratio of HDO and H_2O, respectively, in the vapor phase), and use water vapor and total water to infer P_{vi}, the loss of vapor to ice formation, and S_{wv}, the source of vapor from wall outgassing. The remaining two unknowns are the fractionation α_{eff} and $\gamma \equiv R_w/R_v$, the isotopic composition of wall flux ($R_w = r'_w/r_w$) normalized by that of bulk vapor.

We fit for these unknowns in two ways: fitting α_{eff} and γ independently (two-parameter fit) and assuming that outgassing is nonfractionating sublimation of ice that had previously equilibrated with chamber vapor, i.e., assuming $R_w = \alpha_{\mathrm{eq},0} \cdot R_{v0}$ (one-parameter fit). Results are consistent, suggesting that this assumption is valid. To minimize the influence of wall flux uncertainties, we fit only the initial part of each experiment when ice deposition dominates (54 s to 223 s): most ice growth occurs in the first few minutes of each experiment, and the wall contribution grows over time. See *SI Appendix*, *Fitting Protocol: Individual Experiments* for discussion of fitting individual experiments and uncertainty treatment.

To convert a derived effective fractionation α_{eff} into an equilibrium fractionation α_{eq}, we must assume a functional form for

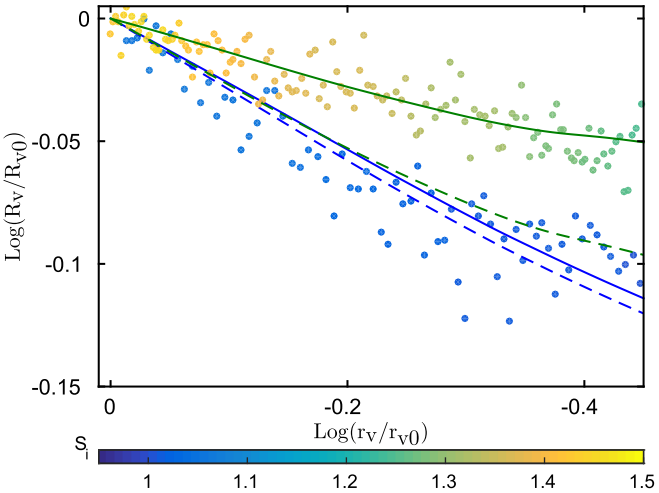

Fig. 3. Example illustrating reduced isotopic partitioning when ice grows in supersaturated conditions. Data points show 1-s measurements of R_v = [HDO]/[H_2O] in two expansion experiments (#27 and #45) at similar temperatures but with differing S_i (mean 1.01 and 1.35), plotted against evolving water mixing ratio r_v. Both axes are scaled to initial values because only relative changes are physically meaningful. The experiment proceeds from upper left to lower right, and the slope gives the effective fractionation $\alpha_{\mathrm{eff}} - 1$. Deviations from linearity result from changing S_i (and thus α_{k}), from changing temperature (and thus α_{eq}), and from wall flux. The two experiments show different effective fractionation (solid lines) but similar derived equilibrium fractionation (dashed lines).

α_k. We take as our default assumptions the classical model of Jouzel and Merlivat (27) (Eq. **2**) and isotopic diffusivity ratio d from Cappa et al. (30), but validate both assumptions using experiments in differing conditions of saturation and ice particle sizes. (See *Results* and *SI Appendix*, *Evaluation of Kinetic Models*.)

To derive the temperature dependence of the equilibrium fractionation factor, we first evaluate equilibrium fractionation factors for all 28 individual experiments, assuming evolving α_k from measured S_i and Eq. **2**. Because the experiments are performed at different temperatures, we can then estimate the temperature-dependent $\alpha_{eq}(T)$ by taking a weighted global fit of the 28 experimental α_{eq} values to the $1/T^2$ temperature dependence of Eq. **1**, constraining the fit to agree with the warmest measurement of Merlivat and Nief (22). (See *SI Appendix, Global Fit Procedure* for details; analysis implies that the functional form of Eq. **2** is indeed valid over this temperature range.)

Results

Equilibrium Fractionation Factor. We find that the temperature dependence of α_{eq} lies far below E13 (26), and slightly below the widely used M67 (22) (Fig. 4). The distinction from M67 (22) is significant to a 3σ confidence interval and robust to assumptions made in fitting and in modeling kinetic isotope effects. (The uncertainty estimates in Fig. 4 are used in weighting the global fit; see *SI Appendix, Fitting Protocol: Individual Experiments* for uncertainty, *SI Appendix, Fitting Protocol: Temperature Dependence* for global fitting, and *SI Appendix, Evaluation of Kinetic Models* for tests of kinetic models.) Estimates for $\alpha_{eq}(T)$ obtained by the two fitting methods differ by $< 10^{-2}$ throughout the experimental temperature range. We recommend that modelers use derived constants for the one-parameter fit: $a_0 = -0.0559$ and $a_1 = 13{,}525$; compare to M67 (22) with $a_0 = -0.0945$ and $a_1 = 16{,}289$.

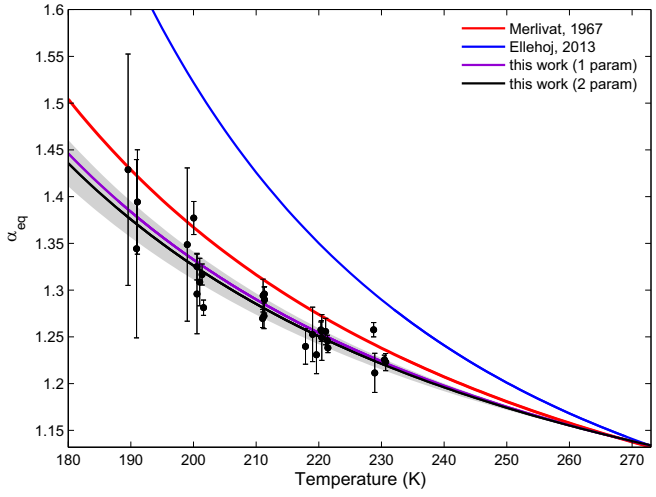

Fig. 4. Equilibrium vapor–ice fractionation factor for HDO/H_2O (α_{eq}) derived from 28 individual IsoCloud experiments. Black and purple lines show global fits through all experiments for two data treatments (black: one-parameter fit, wall flux composition R_w assumed to be that of ice initially at equilibrium with chamber vapor; purple: two-parameter fit, R_w as independent parameter). Dots show individual experiments (one-parameter), and gray shading shows the 3σ confidence interval on the global fit. Error bars represent 2σ uncertainties in fits to individual experiments. (These underestimate experimental error at warmer temperatures; see *SI Appendix, Fitting Protocol: Individual Experiments*.) Solid lines show M67 (ref. 22, red) and E13 (ref. 26, blue); these are derived from experiments at $T > 240$ K and 233 K, respectively. (See *SI Appendix*, Fig. S1 for experimental temperature ranges and all prior estimates of α_{eq}.) Results imply slightly weaker temperature dependence of α_{eq} than with M67 (22).

Kinetic Isotope Effects. As discussed previously, the inferred equilibrium fractionation values of Fig. 4 required correction for assumed kinetic modification, because any supersaturated conditions lead to lower effective isotopic fractionation (Fig. 3). The fact that IsoCloud experiments span a range of supersaturations allows us to quantitatively test models of kinetic isotope effects. Because equilibrium fractionation should depend only on temperature, a validity test for a kinetic model is that retrieved α_{eq} in individual experiments be independent of supersaturation: any dependence on S_i would imply an overcorrection or undercorrection for kinetic effects. We find that if α_k is estimated with the classic diffusive model of Eq. **2** and our default d = 1.0164 (30), the resulting fitted values for α_{eq} indeed show negligible dependence on supersaturation.

We can then extend this test to derive constraints on physical parameters in models of the kinetic effect. In each test case, we find the parameter value that yields a consistent α_{eq} independent of S_i, along with 1σ bounds from propagation of uncertainties. (See *SI Appendix*, *Evaluation of Kinetic Models* for details.) Estimating the isotopic diffusivity ratio d under the pure diffusive model of Eq. **2** yields an optimal value slightly below the lowest published measurement, although with uncertainty encompassing all literature values (Fig. 5). The optimized value is 1.009 ± 0.036, whereas published estimates of d evaluated at 190 K span 1.015 to 1.045 (*SI Appendix*, Table S5). Although this constraint is not strong, it motivates our choice of the relatively low diffusivity ratio measured by Cappa et al. (30) as our default, a value that is also consistent with kinetic gas theory.

We next test a model that incorporates surface kinetic effects following Nelson (29) (*SI Appendix*, Fig. S10). In this model, the isotopic diffusivity ratio d in Eq. **2** is replaced by $(\mathrm{d}k + \mathrm{xy})/(1 + k)$, where x is the ratio of deposition coefficients, y is the ratio of thermal velocities ($\sqrt{19/18}$), and the dimensionless coefficient $k \equiv rv\beta/4D_v$, where r is the ice particle radius and v, D_v, and β are the thermal velocity, diffusivity in air, and deposition coefficient for H_2O, respectively. Note that this surface kinetic model does not reduce to the pure diffusive model of Eq. **2** when x is set to 1 but, when fit to the experiments described here, produces nearly identical results. The limited IsoCloud experiments do not allow d and x to be constrained simultaneously, but we can estimate each given an assumption about the other. We therefore optimize for x in the surface kinetic model given a variety of assumed d.

These tests yield x slightly below 1 regardless of the assumed diffusivity ratio. At the low default d = 1.0164, we obtain $\mathrm{x} = 0.957 \pm 0.22$ (*SI Appendix*, Fig. S10). The higher the assumed value of d, the lower the implied value of x; for example, d = 1.0251 (40) yields x = 0.924 (again $\pm$ 0.22). These experiments may therefore provide tighter constraints on x than the range of 0.8 to 1.2 suggested by Nelson (29). The results consistently suggest that HDO molecules are slightly more likely to be incorporated into the crystal lattice than are H_2O.

Discussion

Given the extensive use of water isotopic variations in climate, atmospheric, and planetary studies, the paucity of measurements of the fundamental fractionation properties of water has long been a concern. This concern was heightened by the recent significant proposed revision by Ellehøj et al. (26) to the half-century-old measurements of Merlivat and Nief (22). The experiments described here should provide some resolution of that discrepancy. The IsoCloud campaign allowed direct measurements of the equilibrium fractionation factor between HDO and H_2O at the cold temperatures characteristic of cirrus clouds, polar snow, or Martian snow and ice deposits. These measurements rule out the substantial upward revision to α_{eq} proposed by Ellehøj et al. (26) and, in fact, imply a slightly weaker temperature

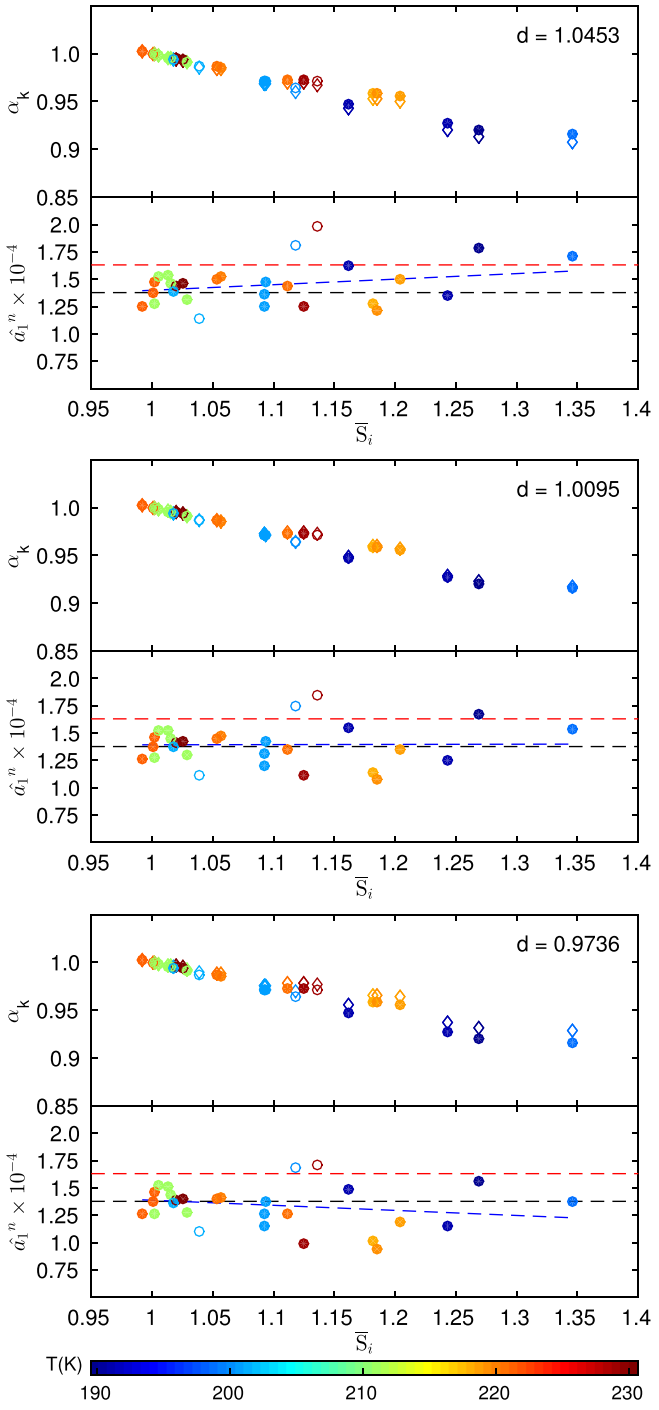

Fig. 5. Effect of choice of d (ratio of isotopic diffusivities) on calculated kinetic effects and retrieved equilibrium fractionation in experiments, plotted against deposition-weighted supersaturation. Top halves of panels show kinetic factors for different experiments using the diffusive model of Jouzel and Merlivat (27) and the stated value of d (circles), and, for reference, identical calculations using the default d = 1.0164 (open diamonds). Bottom halves show resulting equilibrium fractionations, for each experiment, as the a_1 parameters estimated in fitting each experiment n to Eq. **1**, assuming the same constraint as in the global fit. (See *SI Appendix, Tests of Kinetic Models* and Fig. S9.) Deviation from slope 0 implies a misspecified kinetic model. Dashed lines show a_1 values corresponding to M67 (ref. 22, red) and this work (black). Blue line is weighted fit to $\hat{a}_1^n$, excluding three outlier experiments (#4, #26, and #48, shown as open circles). The three panels show the fitted optimal value for d and conservative upper and lower bounds. Bounds span the range of published estimates of d. (See *SI Appendix*, Fig. S10 for similar analysis on x, the ratio of isotopic deposition coefficients.)

dependence and therefore slightly lower equilibrium fractionation than that of Merlivat and Nief (22).

The IsoCloud campaign also provided quantitative confirmation of theories of the kinetic modification to fractionation during ice deposition. Cirrus formation experiments in supersaturated conditions demonstrate that the diffusive model for kinetic isotope effects originally proposed 3 decades ago provides an adequate explanation of suppressed fractionation when ice growth is diffusion-limited. Experiments show slightly weaker kinetic effects than expected with the perhaps most widely used estimate of the isotopic diffusivity ratio (d = 1.0251 from ref. 40) but are consistent with the slightly lower estimate of Cappa et al. (d = 1.0164) (30).

Experimental results are also consistent with a surface kinetic model that posits additional modifications to fractionation due to isotopic differences in incorporation into the ice lattice. Fits to this model consistently suggest a slightly higher deposition coefficient for HDO than for H_2O, although the results cannot exclude equal values. However, the limited set of IsoCloud experiments allows for multiple solutions: an even stronger surface effect favoring HDO deposition could be counteracted by an even stronger diffusion effect preferentially bringing H_2O to the growing ice particle.

The constraints on diffusivity and deposition ratios obtained here could be tightened further given a targeted series of experiments. In IsoCloud, the experiments with conditions most sensitive to kinetic effects tended to be those at the coldest temperatures, where signal-to-noise is lowest. Diffusion-related effects play a role only in supersaturated conditions; in the IsoCloud experiments, homogeneous nucleation experiments with high S_i were conducted only at $T < 205$ K. Surface effects play a role only when k and therefore ice crystal size are small; in IsoCloud, these conditions again occurred only at the coldest temperatures. Values for k (2 to 15) followed ice particle diameters (2 μm to 14 μm), which followed temperature; in IsoCloud, diameters below 5 μm dominated only for $T < 215$ K. New experiments at warmer (> 220 K) temperatures that systematically varied ice crystal diameters in high-supersaturation conditions could allow distinguishing diffusion from surface effects.

Note that, although these methods can, in principle, be used to evaluate fractionation in other isotopologues of water, the oxygen-substituted isotopic systems are more challenging because of their smaller vapor pressure isotope effects: at 190 K, $\alpha_{eq} < 1.04$ for $H_2^{18}O/H_2O$ vs. 1.4 for HDO/H_2O (41). Isotopic doping is, however, particularly useful for the low-natural-abundance $H_2^{17}O$.

Although the particular set of IsoCloud experiments provides only broad constraints on kinetic isotope effects, they demonstrate the potential of in situ vapor measurements in dynamic condensation experiments for diagnosing fundamental isotope physics. All previous approaches to determining equilibrium and kinetic isotopic fractionation in water relied on setting up static conditions and measuring differences or gradients in space. We demonstrate here the power of measuring, instead, evolution over time, in conditions more analogous to condensation in real naturally occurring systems. IsoCloud results show that chamber-based simulations of ice growth in cirrus clouds can provide robust estimates of equilibrium fractionation in the vapor–ice system, and robust constraints on kinetic effects. We hope this approach helps enable further measurements of the fundamental isotopic properties of water and other condensable species.

ACKNOWLEDGMENTS. The many IsoCloud participants contributed greatly to the success of the campaign, including Stephanie Aho, Jan Habig, Naruki Hiranuma, Erik Kerstel, Benjamin Kühnreich, Janek Landsberg, Eric Stutz, Steven Wagner, and the AIDA technical staff and support team. Marc Blanchard provided data from Pinilla et al., 2014 (42) for the comparison of *SI Appendix*, Fig. S1. We thank Thomas Ackerman, Marc Blanchard, Peter Blossey, Won Chang, Albert Colman, Nicolas Dauphas, John Eiler,

Edwin Kite, and William Leeds for helpful discussions and comments. Funding for this work was provided by the National Science Foundation (NSF) and the Deutsche Forschungsgemeinschaft through International Collaboration in Chemistry Grant CHEM1026830. K.D.L. acknowledges support from a National Defense Science and Engineering Graduate Fellowship and an NSF Graduate Research Fellowship, and L.S. acknowledges support from a Camille and Henry Dreyfus Postdoctoral Fellowship in Environmental Chemistry.

1. Jouzel J, Koster RD (1996) A reconsideration of the initial conditions used for stable water isotope models. *J Geophys Res Atmos* 101:22933–22938.
2. Bony S, Risi C, Vimeux F (2008) Influence of convective processes on the isotopic composition (δ^{18}O and δD) of precipitation and water vapor in the tropics: 1. Radiative-convective equilibrium and Tropical Ocean-Global Atmosphere-Coupled Ocean-Atmosphere Response Experiment (TOGA-COARE) simulations. *J Geophys Res Atmos* 113:D19305.
3. Gedzelman SD, Arnold R (1994) Modeling the isotopic composition of precipitation. *J Geophys Res Atmos* 99:10455–10471.
4. Risi C, Bony S, Vimeux F (2008) Influence of convective processes on the isotopic composition (δ^{18}O and δD) of precipitation and water vapor in the tropics: 2. Physical interpretation of the amount effect. *J Geophys Res Atmos*113:D19306.
5. Moyer EJ, Irion FW, Yung YL, Gunson MR (1996) ATMOS stratospheric deuterated water and implications for troposphere-stratosphere transport. *Geophys Res Lett* 23:2385–2388.
6. Hanisco TF, et al. (2007) Observations of deep convective influence on stratospheric water vapor and its isotopic composition. *Geophys Res Lett* 34:L04814.
7. Randel WJ, et al. (2012) Global variations of HDO and HDO/H_2O ratios in the upper troposphere and lower stratosphere derived from ACE-FTS satellite measurements. *J Geophys Res Atmos* 117:D06303.
8. Blossey PN, Kuang Z, Romps DM (2010) Isotopic composition of water in the tropical tropopause layer in cloud-resolving simulations of an idealized tropical circulation. *J Geophys Res Atmos* 115:D24309.
9. Bolot M, Legras B, Moyer EJ (2013) Modelling and interpreting the isotopic composition of water vapour in convective updrafts. *Atmos Chem Phys* 13:7903–7935.
10. Montmessin F, Fouchet T, Forget F (2005) Modeling the annual cycle of HDO in the Martian atmosphere. *J Geophys Res Planets* 110:E03006.
11. Villanueva G, et al. (2015) Strong water isotopic anomalies in the Martian atmosphere: Probing current and ancient reservoirs. *Science* 348:218–221.
12. Sayres DS, et al. (2010) Influence of convection on the water isotopic composition of the tropical tropopause layer and tropical stratosphere. *J Geophys Res Atmos* 115:D00J20.
13. Herbin H, Coheur PF, Hurtmans D, Clerbaux C (2007) Tropospheric water vapour isotopologues ($H_2^{16}O$, $H_2^{18}O$, $H_2^{17}O$ and HDO) retrieved from IASI/METOP data. *Atmos Chem Phys* 7:3957–3968.
14. Worden J, et al. (2012) Profiles of CH_4, HDO, H_2O, and N_2O with improved lower tropospheric vertical resolution from Aura TES radiances. *Atmos Meas Tech* 5:397–411.
15. Nassar R, et al. (2007) Variability in HDO/H_2O abundance ratios in the tropical tropopause layer. *J Geophys Res Atmos* 112:D21305.
16. Steinwagner J, et al. (2007) HDO measurements with MIPAS. *Atmos Chem Phys* 7:2601–2615.
17. Urban J, et al. (2007) Global observations of middle atmospheric water vapour by the Odin satellite: An overview. *Planet Space Sci* 55:1093–1102.
18. Vandaele A, et al. (2011) NOMAD, a spectrometer suite for nadir and solar occultation observations on the ExoMars Trace Gas Orbiter. *Mars Atmosphere: Modelling and Observation*, eds Forget F, Millour M (Lab Metereol Dyn, Paris), pp 484–487.
19. Joussaume S, Sadourny R, Jouzel J (1984) A general circulation model of water isotope cycles in the atmosphere. *Nature* 311:24–29.
20. Jouzel J, et al. (1987) Simulations of the HDO and $H_2^{18}O$ atmospheric cycles using the NASA GISS general circulation model: The seasonal cycle for present-day conditions. *J Geophys Res Atmos* 92:14739–14760.
21. Lee JE, Fung I, DePaolo DJ, Henning CC (2007) Analysis of the global distribution of water isotopes using the NCAR atmospheric general circulation model. *J Geophys Res Atmos* 112:D16306.
22. Merlivat L, Nief G (1967) Fractionnement isotopique lors des changements d'état solide-vapeur et liquide-vapeur de l'eau à des températures inférieures à 0°C. *Tellus* 19:122–127.
23. Criss RE (1991) Temperature dependence of isotopic fractionation factors. *Stable Isotope Geochemistry: A Tribute to Samuel Epstein*, eds Taylor HP, O'Neil JR, Kaplan IR (Geochem Soc, Washington, DC), Vol 3, pp 11–16.
24. Dauphas N, Schauble E (2016) Mass fractionation laws, mass-independent effects, and isotopic anomalies. *Annu Rev Earth Planet Sci* 44:709–783.
25. Bigeleisen J, Mayer M (1947) Calculation of equilibrium constants for isotopic exchange reactions. *J Chem Phys* 15:261–267.
26. Ellehøj MD, Steen-Larsen HC, Johnsen SJ, Madsen MB (2013) Ice-vapor equilibrium fractionation factor of hydrogen and oxygen isotopes: Experimental investigations and implications for stable water isotope studies. *Rapid Commun Mass Spectrom* 27:2149–2158.
27. Jouzel J, Merlivat L (1984) Deuterium and oxygen 18 in precipitation: Modeling of the isotopic effects during snow formation. *J Geophys Res* 89:11749–11757.
28. Dansgaard W (1964) Stable isotopes in precipitation. *Tellus* 16:436–468.
29. Nelson J (2011) Theory of isotopic fractionation on facetted ice crystals. *Atmos Chem Phys* 11:11351–11360.
30. Cappa CD, Hendricks MB, DePaolo DJ, Cohen RC (2003) Isotopic fractionation of water during evaporation. *J Geophys Res Atmos* 108:11351.
31. Uemura R, Matsui Y, Yoshida N, Abe O, Mochizuki S (2005) Isotopic fractionation of water during snow formation: Experimental evidence of kinetic effect. *Polar Meteorol Glaciol* 19:1–14.
32. Casado M, et al. (2016) Experimental determination and theoretical framework of kinetic fractionation at the water vapour-ice interface at low temperature. *Geochim Cosmochim Acta* 174:54–69.
33. DePaolo D (2011) Surface kinetic model for isotopic and trace element fractionation during precipitation of calcite from aqueous solutions. *Geochim Cosmochim Acta* 75:1039–1056.
34. Takahashi T, Endoh T, Wakahama G, Fukuta N (1991) Vapor diffusional growth of free-falling snow crystals between -3 and -23°C. *J Meteorol Soc Jpn Ser* 69:15–30.
35. Nelson J (2005) Branch growth and sidebranching in snow crystals. *Crystal Growth Design* 5:1509–1525.
36. Möhler O, et al. (2003) Experimental investigation of homogeneous freezing of sulphuric acid particles in the aerosol chamber aida. *Atmos Chem Phys* 3:211–223.
37. Möhler O, et al. (2006) Efficiency of the deposition of mode ice nucleation on mineral dust particles. *Atmos Chem Phys* 6:3007–3021.
38. Cziczo D, et al. (2013) Ice nucleation by surrogates of Martian mineral dust: What can we learn about Mars without leaving Earth? *J Geophys Res Planets* 118:1945–1954.
39. Cotton RJ, Benz S, Field P, Möhler O, Schnaiter M (2007) Technical note: A numerical test-bed for detailed ice nucleation studies in the aida cloud simulation chamber. *Atmos Chem Phys* 7:243–256.
40. Merlivat L (1978) Molecular diffusivities of $H_2^{16}O$, $HD^{16}O$, and $H_2^{18}O$ in gases. *J Chem Phys* 69:2864–2871.
41. Majoube M (1971) Fractionation in O-18 between ice and water vapor. *J Chim Phys Phys Chim Biol* 68:625–636.
42. Pinilla C, et al. (2014) Equilibrium fractionation of H and O isotopes in water from path integral molecular dynamics. *Geochemica et Cosmochemica Acta* 135:203–216.

Supplementary Online Material

Laboratory measurements of HDO/H_2O isotopic fractionation during ice deposition in simulated cirrus clouds

Kara D. Lamb[1], Benjamin W. Clouser[1], Maximilien Bolot[2], Laszlo Sarkozy[2], Volker Ebert[3], Harald Saathoff[4], Ottmar Möhler[4], Elisabeth J. Moyer[2]

1. Dept. of Physics, University of Chicago
2. Dept. of the Geophysical Sciences, University of Chicago
3. Physikalisch-Technische Bundesanstalt
4. Institute for Meteorology and Climate Research, Karlsruhe Institute of Technology

Contents

S1 Review of previous determinations of α_{eq}

A total of eight previous works have attempted to determine the fractionation factor for vapour over ice for the HDO to H_2O system, five experimental measurements and three theoretical calculations. See Table S1 for summary and Figure S1 for plot.

The measurements can be roughly categorized as "indirect" or "direct" measurements. In the three indirect measurements, the quantities measured are typically the vapour pressures over D_2O and H_2O ice, and the fractionation factor is derived by assuming the law of geometric means [1, 2]. In the two previous direct measurements, fractionation between phases is determined by measuring the isotopic ratio in a vapour stream at two points, before and after vapour comes into contact with an ice surface and presumably reaches equilibrium with it. Theoretical values are derived from molecular modeling approaches that use different methods. Each modeling method involves approximations, and neither is expected to provide tight constraints on the fractionation factor.

Measurement	**Temp. Range**	**Type**	**Method**
Matsuo, et al., 1964 [3]	235 - 273 K	Experimental (indirect)	Vapour pressure, D_2O and H_2O
Merlivat and Nief, 1967 [4]	233 - 273 K	Experimental (direct)	Mass spectrometry
Van Hook, 1968 [5]	233 - 273 K	Theoretical	Effective force field
Johansson et al. 1969 [6]	253 - 273 K	Experimental (indirect)	Specific heat, latent heat
Pupezin et al., 1972 [7]	209 - 273 K	Experimental (indirect)	Vapour pressure, D_2O and H_2O
Méheut et al., 2007 [8]	203 - 273 K	Theoretical	Density functional theory
Ellehøj et al., 2013 [9]	223 - 269 K	Experimental (direct)	Mass spectrometry
Pinilla et al., 2014 [10]	190 - 273 K	Theoretical	Empirical force field & Path integral molecular dynamics

Table S1: Previous measurements and theoretical determinations of the equilibrium fractionation factor for vapour over ice for the HDO/H_2O system.

S2 IsoCloud campaign and instruments

The IsoCloud campaigns at the AIDA Cloud Chamber ran from Spring 2012 to Spring 2013, with the first two campaigns dedicated to integration and engineering tests and the final two to science. Instruments participating in these campaigns were provided by research groups from several institutions. Details of instruments used in the analysis are given in S2.1 and instrument placement is shown in Figure S2. All data shown in this work is taken from IsoCloud 4 (March 2013), since low isotopic doping during IsoCloud 3 (October 2012) limited data utility.

The main goals of the IsoCloud campaigns were to

- Develop and test isotopic water vapour instruments in a controlled laboratory setting.
- Measure the equilibrium fractionation factor α_{eq} between vapour and ice in atmospheric conditions typical of the upper troposphere and lower stratosphere.
- Verify kinetic fractionation effects due to diffusion limitation at low temperatures.
- Investigate potential surface inhibition effects that could lead to anomalous supersaturation and could potentially have isotopic implications.
- Investigate potential metastable phases of ice that could form at low temperatures, and could potentially have isotopic implications.

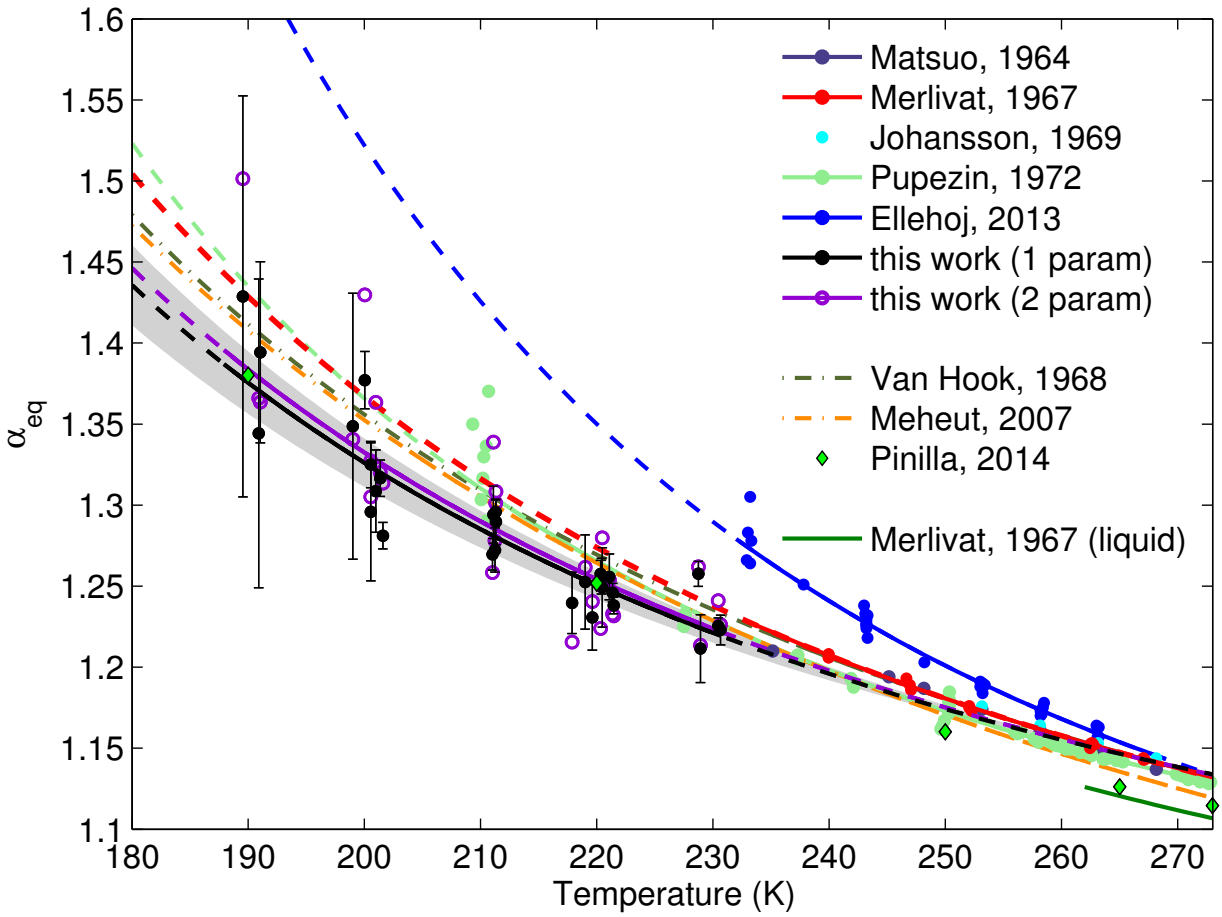

Figure S1: All previous determinations of the fractionation factor between vapour and ice for HDO/H_2O, and new measurements from this work (shown for two fitting cases). For all measurements, dots are experimental values, solid lines are parameterizations derived from those measurements in the experimental temperature range, and dashed lines are extrapolations outside the experimental range. Calculations and parameterizations from theory are shown in diamonds and dashed-dotted lines. (Each modeling method uses different approximations, and are not expected to provide tight constraints on the fractionation factor.) The fractionation factor for the vapour-liquid transition is shown for reference; preferential partitioning in the vapour-liquid system should be less than in the vapour-solid system. Error bars shown for this work are 2σ uncertainties, shown for clarity only on the one-parameter case. We assume identical uncertainties for both cases; see Sections S4-S5 for determination and discussion. These uncertainties are used as weights in fitting for the global temperature dependence of α_{eq}.

S2.1 Instruments used in isotopic analysis

The isotopic ratio measurements used in the analysis are taken from the ChiWIS instrument, but the fractionation factor analysis requires data from water measurements by two other instruments as well and from facility temperature and pressure sensors. Measurements used are summarized in Table S2 and discussed in more detail below.

Exp. Observable	Instrument	Technique
T_{gas}	AIDA sensors	thermocouples
p_{gas}	AIDA sensors	–
HDO/H_2O vapour ratio	ChiWIS	in-situ, TDL multi-pass
H_2O vapour mixing ratio	ChiWIS	in-situ, TDL multi-pass
H_2O vapour mixing ratio	SP-APicT	in-situ, TDL single-pass
Total H_2O (vapour + ice)	APeT	extractive, TDL multi-pass
Ice number density	welas	optical particle counter

Table S2: Experimental observables used to determine α_{eq} during the IsoCloud campaigns. All water measurements are made by tunable diode laser (TDL) absorption spectroscopy. APeT and SP-APicT are AIDA instruments that measure $H_2^{16}O$, and ChiWIS is an isotopic water vapour instrument integrated into AIDA specifically for HDO and $H_2^{16}O$ measurements during IsoCloud.

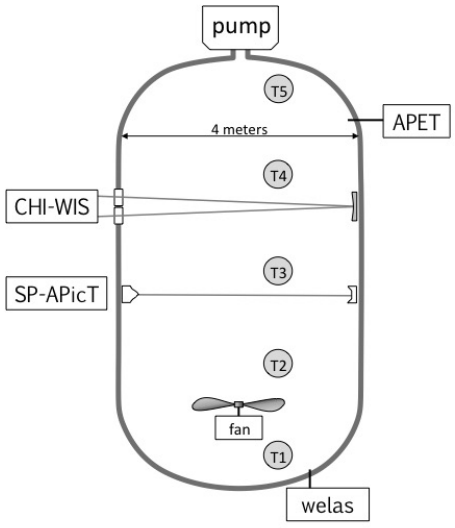

Figure S2: Positioning of the instruments used in this analysis during the IsoCloud experiment campaigns. (Additional instruments also participated in the IsoCloud campaigns.) We take gas temperature as the average of thermocouples T1-4. Data from the welas optical particle counter are used to derive the effective ice particle diameter listed in Table S3 and in calculating kinetic isotope effects.

S2.1.1 AIDA gas temperature and pressure measurements

Gas temperature inside the containment vessel is measured by five thermocouples at different heights along an axis about 1 m from the center of the vessel. (See Figure S2.) We take as the gas temperature the average of the four lowest thermocouples (T1-4); the top of the chamber is less well mixed and experiences fluctuations that are not characteristic of the bulk air being sampled. Mixing is provided by a fan located 1 m above the floor of the chamber. Individual thermocouples show variations of ± 0.3 K during expansion experiments

and ±0.15 K during stable periods between pumpdowns, on timescales of 30 s, likely due to turbulent mixing [11]. These inhomogeneities form an additional source of uncertainty for experiments. Gas temperatures and pressures are used in calculation of spectral line shapes, saturation vapour pressure, and in the conversion of number density to mixing ratio.

S2.1.2 APeT total water measurement

APeT (AIDA PCI extractive TDL) is a tunable diode laser absorption spectrometer permanently installed at the facility. It measures total water (ice and vapour) by extracting gas from the chamber through a heated inlet [12, 13]. We assume a 17 second delay in the APeT extractive measurements based on previous comparison of *in situ* and extractive instruments [13]. This delay is consistent with the timing of observed changes in isotopic ratio during IsoCloud pumpdowns. We use total water to determine the rate of deposition of vapour to ice, the contribution of vapour from the chamber walls, and the total ice content.

S2.1.3 SP-APicT water vapour measurement

SP-APicT (single pass AIDA PCI in cloud TDL) is a tunable diode laser absorption spectrometer installed at AIDA that measures *in situ* vapour H_2O with a single-pass configuration (4.1 m pathlength) [13]. Because the SP-APicT optical path involves no reflections, the measurement is not affected by backscattering from chamber ice particles. Water vapour measurements from ChiWIS to SP-APicT show a consistent ratio of ∼1.025 in no-cloud conditions at temperatures above 205 K, likely the result of systematic error in the linestrengths used in retrievals for one or both instruments [14, 15]. (At lower temperatures, water content is below the SP-APicT dynamic range.) SP-APicT is used for backscattering corrections to ChiWIS water vapour and vapour isotopic ratio in experiments with dense ice clouds.

S2.1.4 welas particle counters

The welas instruments are optical particle counters that can measure ice particle number concentrations for particles in a specified size range. Two instruments were used during the IsoCloud campaigns, with effective spherical size ranges of 0.7–46 and 5–240 μm [16], time resolution of 5 s, and accuracy estimated at ±20 % [17]. (Uncertainty is for the measured number concentration, which is mainly due to the uncertainty of the detection volume size inside the optical particle counters.) In this analysis, welas data are used to approximate effective ice crystal radii for use in the kinetic fractionation model that includes surface kinetic effects.

S2.1.5 ChiWIS H_2O and HDO measurements

The Chicago Water Isotope Spectrometer (ChiWIS) is a tunable diode laser absorption spectrometer that scans across both HDO and H_2O spectral lines, allowing for a simultaneous retrieval of the concentration of both isotopologues in the vapour phase inside AIDA. The spectrometer is used in a non-resonant multi-pass White Cell configuration (set between 196.3–256.5 m) inside the cloud chamber, allowing for *in-situ* measurements of the evolving

isotopic composition inside AIDA [18, 19]. The instrument design, data acquisition, fitting, and performance during the IsoCloud campaigns are described in detail in [20].

The dynamic range of ChiWIS for isotopic measurements in IsoCloud conditions is ∼0.5–400 ppm water at pressures ∼100–300 mb (producing 0.06–39% absorption for H_2O and 0.03–19% for HDO doped 15x). Measurements of isotopic composition are limited at high temperatures by saturation of the H_2O line and at low temperatures by signal-to-noise on the HDO line. (The low-temperature limit could be modified by higher isotopic doping levels.) We apply a calibration to ChiWIS measurements during some IsoCloud experiments with ice clouds dense enough that backscattered light onto the detector produces artifacts. The dominant effect of dense ice clouds is to reduce total laser power reaching the ChiWIS detector (by up to 95%), but a secondary effect is that some light scatters back onto the detector after traversing a shorter distance than the intended optical pathlength. That backscattered contribution reduces all apparent line depths. If laser power at the position of HDO and H_2O lines were identical, any modification would be identical for both species and would not affect their ratio. In actuality, the H_2O and HDO lines are affected slightly differently. Since SP-APicT is not affected by backscattering, we identify the experiments that may experience artifacts by comparing measured concentrations of H_2O by SP-APicT and ChiWIS. When needed (17 of 28 experiments), we use a simple model to reconstruct ChiWIS spectra without contributions from backscattered light. Under the harshest experimentally realized conditions, the applied correction to the isotopic ratio is 0.22% out of a total ratio decline of 13.2% (at 225 K; see Table S3). (The adjustment on water vapour alone is larger, with maximum value 11%.) At lower temperatures, water vapour content in the chamber is too small to produce clouds thick enough to cause deviations in absorption spectra.

Our backscatter correction model assumes that backscattered light has a path length so short that it can be approximated as an absorption-free offset to the raw data. For each spectrum recorded, we calculate the effect on the isotopic ratio using synthetic spectra.

First, we verify that the ratio between ChiWIS and SP-APicT is identical before and after the presence of ice particles. We then fit the raw spectral data to a model that assumes the true concentration is given by SP-APicT scaled up by this ratio, and that the spectrum of the main beam sits atop a frequency-independent offset introduced by backscatter into the detector. The size of this offset is the only free parameter in this fit. We then remove the calculated offset from the ChiWIS data and re-fit for the HDO concentration.

The robustness of the procedure is demonstrated by the relative consistency of inferred fractionation factor values at a given temperature. Because ice cloud properties vary between pumpdowns, each temperature cluster of experiments involves different degrees of influence from backscatter. We see no evidence of systematics in the final calibrated data.

S2.2 Preparation of AIDA for isotopic measurements

AIDA was chosen as a setting for an isotopic water measurement campaign because of its extensive history of use for cirrus experiments, its well-characterized facility instruments, and its large volume (84 m^3), which mediates wall effects. On each of nine experimental days (4-6 individual pumpdowns) the AIDA chamber wall temperature remained approximately constant. Between experimental days, chamber temperature was adjusted at night (typical rates ∼4 K/h) to a new setpoint. To test for any systematics, some temperatures were

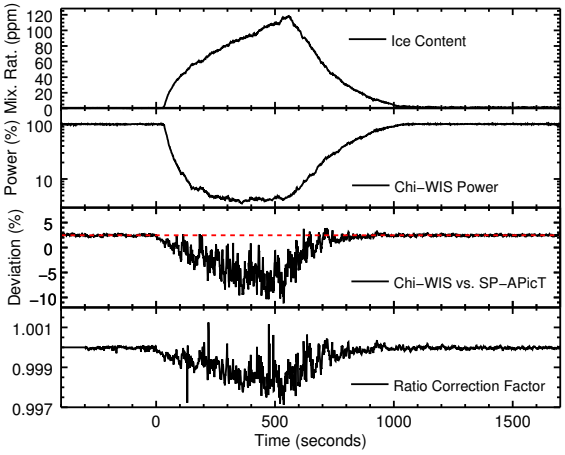

Figure S3: Example of a pumpdown in thick ice cloud conditions (Experiment #8; the most extreme case). Time 0 marks the start of pumping; ice formation begins ∼20 seconds after and grows rapidly, attenuating the collected ChiWIS power, with peak loss ∼95%. Power recovers as the ice cloud dissipates, indicating that no change in instrument alignment has occurred. ChiWIS H_2O is typically 2.5% above that in SP-APicT; as ice content grows, ChiWIS drops relative to SP-APicT. The applied isotopic ratio correction is much smaller than that for water vapour (max 0.22%) since HDO and H_2O are affected similarly. Ice content is determined using APeT total water.

repeated on multiple days, so the total campaign comprises 6 temperature groupings, 3 of which were repeated. During IsoCloud 4, chamber preparation followed standard procedure with some special adaptations for isotopic water measurements, described in more detail below. During most of the IsoCloud 4 campaign, the chamber was prepared with ice-covered walls to ensure a known isotopic composition of flux from the walls. Both wall ice and water vapour in the cloud chamber were isotopically doped above natural abundance to provide a larger signal for isotopic measurements. On one experimental day, all pumpdowns were conducted with dry walls.

Chamber preparation. At the end of each experiment day, the chamber is purged with a pump-and-flush cycle: eight times first pumping out to 1 hPa, then filling with synthetic dry air at 10 hPa. The chamber is then pumped out completely to a pressure of ∼0.01 hPa to remove all aerosols. (Background aerosol concentrations are typically < 0.1 particle per cm^{-3}.) In the morning of the next experimental day, the desired amount of water vapour for the next experiment is added to the chamber by opening a valve leading (via a heated stainless steel tube) to a heated water reservoir containing nanopure-quality water with isotopic composition enriched in HDO by approximately ×10-20 and in $H_2^{18}O$ by approximately ×2 compared to natural abundance (VSMOW) [21, 22, 23]. (HDO enrichment is achieved by adding D_2O, which then partitions statistically.) After water addition, the chamber is filled with dry synthetic air (N_2 and O_2 only) up to the desired pressure for the first experiment. Most experimental days in IsoCloud 4 begin with a "reference pumpdown" with essentially no ice nuclei present, so that no condensation occurs. Aerosols are then added to ensure formation of ice crystals in all subsequent pumpdowns.

Ice-covered wall preparation. On most days, sufficient water is injected into the chamber to not only saturate chamber air but also to form a thin coating of ice on chamber walls. (The wall temperatures are typically ∼ 0.3 to 0.9 K lower than chamber air temperature). If the ice coating were uniform, the total amount would correspond to a layer ∼2 μm thick on the 110 m^2 chamber surface. In practice, non-uniform wall temperatures may produce an inhomogeneous ice layer [24]. The ice layer serves as a water source that recharges the chamber following each pumpdown. When the chamber is static, the walls maintain the

chamber air at between 80-85% of saturation vapour pressure, since wall temperatures are slightly lower than chamber air temperature. After a pumpdown, once ice particles in the chamber have fully sublimated, chamber water vapour and the isotopic ratio of the gas re-equilibrates with the walls on a timescale of ∼5 minutes. In our data analysis, fits of the isotopic composition of the wall outgassing component are consistent with the isotopic signature of ice that had been in equilibrium with chamber vapour before the pumpdown.

Dry wall preparation. As a test, one experimental day (experiments #39-43) was conducted with bare aluminum walls. On this day, operators added water to the chamber in successive steps until chamber air reached just below saturation vapour pressure at the wall temperature. The chamber was then left static for ∼30 minutes to allow chamber vapour and walls to equilibrate. After each pumpdown (with attendant loss of water), water was again added to bring the chamber close to saturation. Dry-wall pumpdowns feature a lower proportion of chamber vapour depositing as ice and smaller changes in vapour isotopic composition.

S2.3 Summary of IsoCloud 4 experiments

The analysis here involves all 28 of the 48 total expansion experiments during IsoCloud 4 that produced useable isotopic ratio measurements during ice cloud formation. These data were taken on seven different experimental days. (See Table S3 for complete list and Figure S4 for isotopic evolution in individual experiments.)

Of the twenty experiments not analyzed, nine involved insufficient ice deposition: six intentional "reference" pumpdowns with no aerosol or mineral dust addition (#12, 18, 28, 34, 39, and 44), and three cases of unintentional insufficient addition (#2, 19, and 40). (We analyze only experiments in which at least 20% of the initial vapour deposits as ice.) On one experimental day, anomalously high noise on ChiWIS isotopic ratios precluded use of all experiments (#29-33). On the coldest experimental day (189 K), isotopic doping was insufficient for use of HDO measurements, precluding use of experiment #35; for the three following experiments (#36-38), the laser was tuned over a different spectral region to focus on H_2O, foregoing HDO measurements. ChiWIS did not record data during one experiment (#23), and another (#24) began before the ChiWIS laser was stabilized in temperature.

The analysis includes 3 experiments (#41-43) conducted on March 21, the day that the AIDA chamber was prepared with dry walls rather than with an isotopically doped ice layer. Isotopic retrievals from these experiments meet goodness-of-fit criteria but demonstrate significantly higher sensitivity to the choice of region length than experiments with ice-covered walls, including the set of experiments conducted at similar temperature (#6-11, on March 13). That sensitivity is reflected in larger uncertainty in the retrieval of the fractionation factor (Figure S5, top panel.) The isotopic signature of water vapour desorbing from the walls is also not likely to be exactly the value expected for equilibrated ice, implying some bias in the 1-parameter fit assumptions (See S4). In the 1-parameter fit, the dry-wall experiments fit systematically slightly low (Figure S5, bottom panel).

The complete dataset analyzed covers a range of pumpdown start temperatures from 194 to 234 K, producing water vapour mixing ratios between 2 and 380 ppmv. Maximum supersaturations ranged between 1.03 and 1.62, with the highest values in homogeneous nucleation experiments. High-supersaturation experiments are distributed across the temper-

ature range. Our equilibrium fractionation factor retrievals show no systematic dependence on S_i. (See manuscript Figure 5 and Figure S10.)

ID	T_0**(K)**	ΔT**(K)**	p_0 **(hPa)**	Δ**p (hPa)**	w_{eff} **(cm/s)**	$R_{vD,0}$	$\delta R_{vD,0}$ (%)	$r_{v,0}$ **(ppmv)**	$\delta r_{v,0}$ (%)	S_{max}	$\bar{S}_i$	d_{avg} (μm)	**IN**	$R_{vD,dev}$ (%)	r_{dev} (%)
1	**234**	**7.8**	**299**	**65**	**-370**	**16.5**	**8.5**	**380**	**39.0**	**1.21**	**1.12**	**14**	**ATD**	**-0.18**	**5.4**
2	233	6.5	300	100	-130	16.6	4.0	366	17.7	1.24	–	7	ATD	-0.06	1.5
3	**233**	**6.4**	**300**	**101**	**-120**	**17.1**	**6.0**	**377**	**28.6**	**1.03**	**1.02**	**10**	**ATD**	**-0.06**	**1.4**
4	**233**	**9.1**	**300**	**131**	**-130**	**17.4**	**8.7**	**375**	**38.2**	**1.21**	**1.14**	**10**	**ATD**	**-0.09**	**2.4**
5	**233**	**9.1**	**300**	**132**	**-180**	**17.9**	**9.9**	**387**	**43.8**	**1.05**	**1.03**	**11**	**ATD**	**-0.09**	**2.3**
6	**223**	**6.6**	**300**	**71**	**-170**	**13.1**	**6.7**	**113**	**29.0**	**1.27**	**1.20**	**11**	**ATD**	–	–
7	**223**	**6.4**	**234**	**64**	**-140**	**12.7**	**10.6**	**147**	**35.3**	**1.03**	**1.00**	**6**	**ATD**	**-0.17**	**6.3**
8	**223**	**8.7**	**300**	**131**	**-200**	**12.8**	**13.2**	**114**	**46.4**	**1.04**	**1.00**	**8**	**ATD**	**-0.22**	**11.4**
9	**223**	**6.0**	**300**	**71**	**-160**	**13.1**	**8.8**	**114**	**30.7**	**1.12**	**1.06**	**6**	**ATD**	**-0.04**	**2.2**
10	**223**	**5.5**	**231**	**62**	**-130**	**13.1**	**7.7**	**147**	**29.7**	**1.10**	**1.05**	**6**	**ATD**	**-0.16**	**2.9**
11	**223**	**8.9**	**300**	**150**	**-180**	**13.2**	**14.7**	**115**	**47.3**	**1.03**	**0.99**	**7**	**ATD**	**-0.09**	**5.5**
12	213	5.4	298	69	–	–	–	–	–	–	–	–	–	–	–
13	**213**	**5.3**	**234**	**64**	**-130**	**11.5**	**9.6**	**40.6**	**33.1**	**1.06**	**1.03**	**2**	**ATD**	**-0.01**	**1.8**
14	**213**	**8.4**	**300**	**137**	**-160**	**11.9**	**14.4**	**30.9**	**46.8**	**1.04**	**1.00**	**2**	**ATD**	**-0.01**	**2.1**
15	**213**	**5.6**	**300**	**71**	**-160**	**12.0**	**9.7**	**31.3**	**63.4**	**1.04**	**1.01**	**2**	**ATD**	**-0.01**	**2.0**
16	**213**	**5.4**	**234**	**64**	**-140**	**12.1**	**9.5**	**39.9**	**32.1**	**1.03**	**1.02**	**2**	**ATD**	**-0.02**	**2.0**
17	**213**	**8.4**	**300**	**130**	**-150**	**12.2**	**15.6**	**31.1**	**48.3**	**1.04**	**1.01**	**2**	**ATD**	**-0.02**	**3.0**
18	194	–	–	–	–	–	–	–	–	–	–	–	–	–	–
19	194	5.2	300	71	-120	10.9	1.4	1.78	2.2	1.87	–	9	ATD	–	–
20	**194**	**4.8**	**239**	**70**	**-90**	**10.5**	**12.7**	**2.13**	**36.2**	**1.46**	**1.16**	**2**	**ATD**	–	–
21	**194**	**7.6**	**300**	**131**	**-120**	**10.2**	**18.4**	**1.70**	**53.9**	**1.60**	**1.24**	**1**	**ATD**	–	–
22	**194**	**7.4**	**300**	**131**	**-120**	**10.4**	**15.4**	**1.67**	**51.5**	**1.62**	**1.27**	**1**	**ATD**	–	–
23	194	7.0	250	81	-180	–	–	–	–	–	–	–	ATD	–	–
24	204	5.4	304	74	-130	–	–	–	–	–	–	–	ATD	–	–
25	**204**	**4.9**	**233**	**63**	**-100**	**9.4**	**7.9**	**9.98**	**27.8**	**1.20**	**1.09**	**2**	**ATD**	–	–
26	**204**	**8.0**	**300**	**131**	**-130**	**9.7**	**13.1**	**7.72**	**49.0**	**1.27**	**1.12**	**2**	**ATD**	–	–
27	**204**	**8.1**	**300**	**131**	**-160**	**9.8**	**13.8**	**7.58**	**48.4**	**1.07**	**1.02**	**2**	**ATD**	–	–
28	194	5.1	304	75	-120	10.1	3.0	1.60	23.6	1.67	–	4	–	–	–
29	194	6.5	235	66	-140	10.9	4.9	2.04	13.2	1.84	–	6	SA	–	–
30	194	7.6	300	131	-140	10.9	10.5	1.65	53.4	1.88	–	2	SA	–	–
31	194	7.5	300	131	-150	10.5	5.9	1.78	53.3	1.95	–	4	SA	–	–
32	194	7.6	300	131	-140	10.2	6.8	1.74	58.7	1.34	–	2	ATD-SA	–	–
33	194	7.6	300	139	-120	9.3	17.6	1.55	60.4	1.34	–	2	ATD-SA	–	–
34	189	7.3	306	136	-140	10.6	13.6	0.78	21.1	1.84	–	4	–	–	–
35	189	7.3	305	137	-140	9.5	22.8	0.73	60.9	1.88	–	3	SOA	–	–
36	189	7.3	302	134	-150	–	–	0.58	0.26	1.95	–	–	SOA-H	–	–
37	189	7.2	301	132	-140	–	–	0.79	0.47	1.34	–	–	SOA-H	–	–
38	189	7.0	301	135	-120	–	–	0.72	0.32	1.34	–	–	SOA-H	–	–
39	224	6.1	300	71	-120	13.2	0.6	112	1.3	1.24	–	–	–	-0.01	0.4
40	224	7.6	234	65	-120	13.3	3.3	129	14.8	1.18	–	2	ATD	-0.02	0.7
41	**224**	**8.9**	**300**	**134**	**-240**	**13.4**	**7.4**	**103**	**31.4**	**1.24**	**1.18**	**9**	**ATD**	**-0.03**	**1.7**
42	**224**	**8.4**	**300**	**130**	**-160**	**12.2**	**9.1**	**121**	**44.0**	**1.23**	**1.18**	**10**	**ATD**	**-0.04**	**2.7**
43	**224**	**8.5**	**300**	**130**	**-130**	**10.7**	**7.6**	**128**	**40.3**	**1.12**	**1.11**	**9**	**ATD**	**-0.04**	**2.0**
44	204	8.0	300	71	-300	12.8	3.8	7.96	30.8	1.71	–	4	–	–	–
45	**205**	**8.3**	**300**	**134**	**-140**	**12.7**	**7.3**	**7.79**	**34.0**	**1.45**	**1.35**	**4**	**SA**	–	–
46	**204**	**5.5**	**301**	**74**	**-130**	**12.6**	**7.7**	**8.32**	**34.0**	**1.20**	**1.09**	**2**	**SA**	–	–
47	**204**	**5.2**	**233**	**64**	**-120**	**12.7**	**7.2**	**10.1**	**27.5**	**1.17**	**1.09**	**2**	**SA**	–	–
48	**204**	**7.6**	**301**	**132**	**-150**	**12.6**	**11.3**	**8.06**	**48.5**	**1.12**	**1.04**	**2**	**SA**	–	–

Table S3: All adiabatic expansion experiments during IsoCloud 4; the 28 experiments used in this analysis are shown in boldface. Each subsection delineates experiments performed during a single day. Columns show: ID - experiment number; T_0(K) - initial temperature before pumps turn on; ΔT(K) - change in temperature during an experiment; p_0 (hPa) - initial pressure; Δp (hPa) - change in pressure during an experiment; $R_{vD,0}$ - initial isotopic ratio (in terms of natural abundance); $\delta R_{vD,0}$ - change in isotopic ratio due to an experiment; $r_{v,0}$ (ppmv) - initial mixing ratio of H_2O; $\delta r_{v,0}$ (ppmv) - change in mixing ratio due to ice deposition; w_{eff} - cooling rate expressed as an effective updraft speed [24]; S_{max} - maximum saturation during an experiment; $\bar{S}_i$ - deposition weighted average saturation; d_{avg} (μm) - mean diameter; IN - ice nuclei; abbreviated as ATD (Arizona Test Dust), SA (sulfate aerosols), SOA (secondary organic aerosols), and SOA-H (secondary organic aerosols plus nitric acid); $R_{vD,dev}$ - maximum fractional correction on isotopic ratio due to backscattering during a pumpdown; r_{dev} - maximum fractional correction on mixing ratio of H_2O due to backscattering correction during a pumpdown. (The maximum corrections in last two columns generally exceed those in the experimental regions analyzed.)

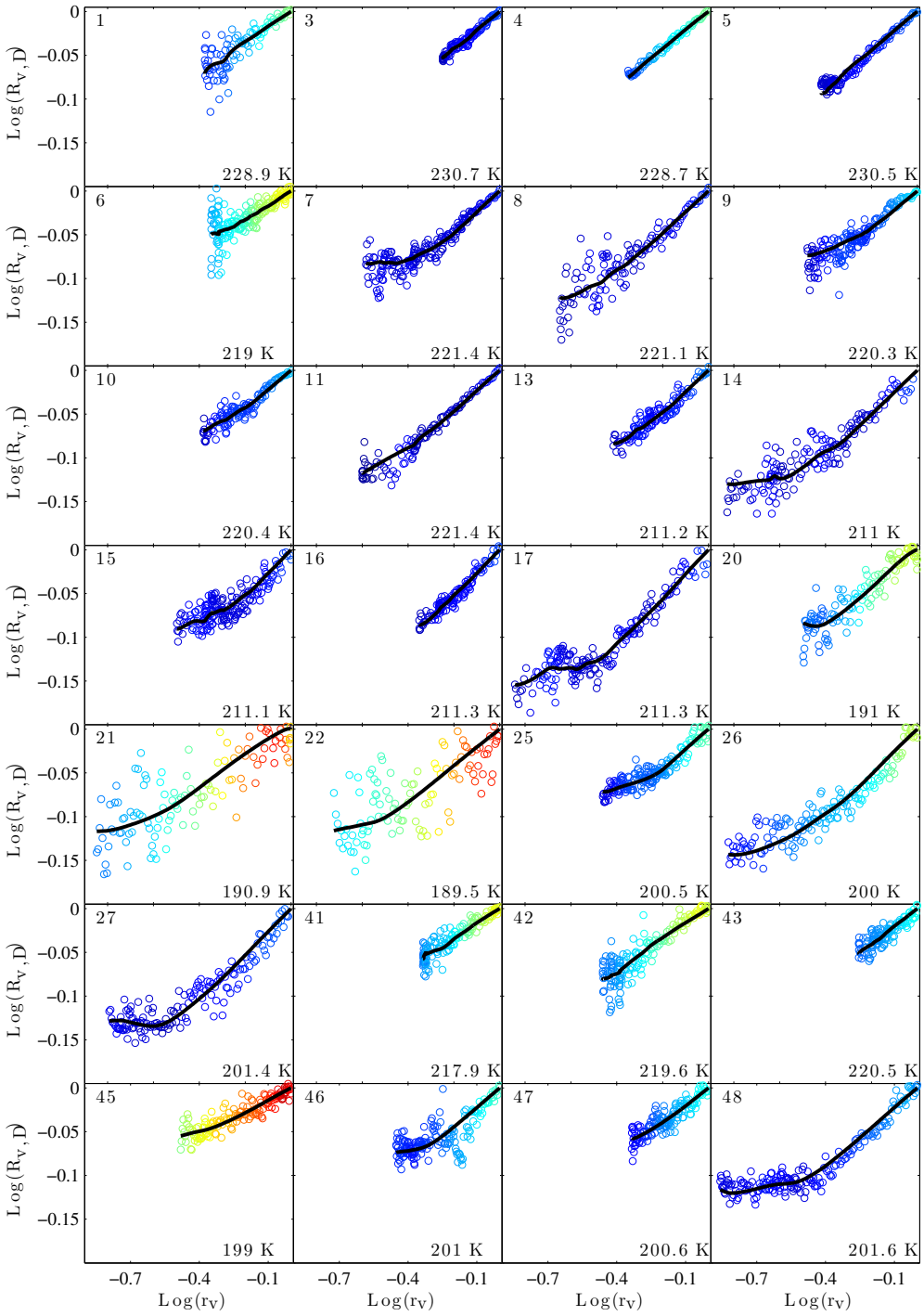

Figure S4: Isotopic evolution in all adiabatic expansion experiments used in this analysis. Points represent measured data during the defined analysis region, colored by degree of supersaturation with respect to ice. (Color scale from blue to red indicates S_i of 0.95 to 1.5.) Black line shows the best-fit model of isotopic evolution, as described in Section S4. Time evolution in each experiment proceeds from top right to lower left, with the initial slope giving $\alpha_{\text{eff}} - 1$. Temperature at lower right in each panel is the initial temperature in each analysis region (several degrees lower than the pumpdown start temperature listed in Table S3).

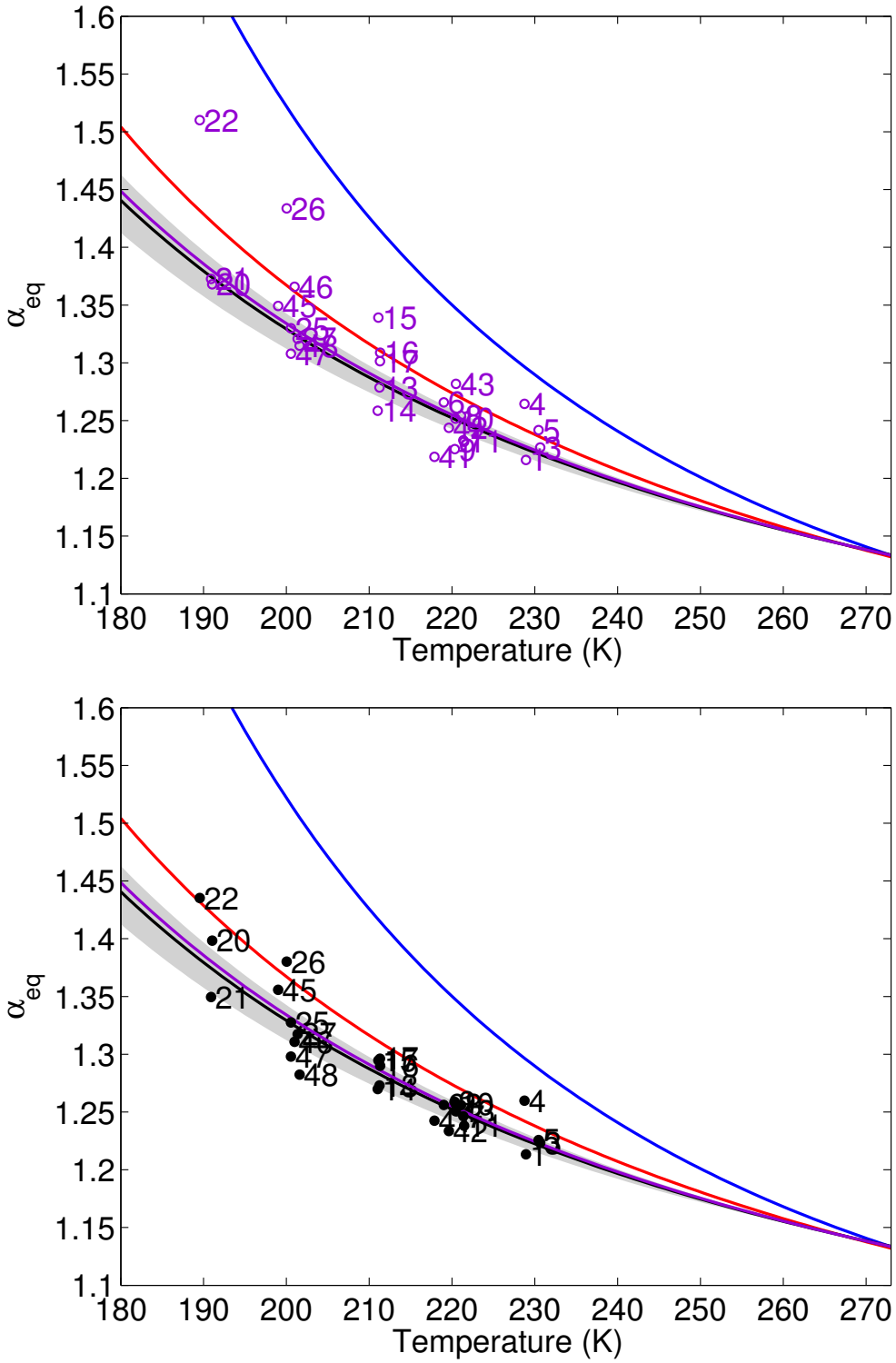

Figure S5: Fits for α_{eq}, identified by experiment number. **Top:** the 2-parameter case, and **bottom:** the 1-parameter case. Black and purples lines show the corresponding global fits, and blue and red lines show the E13 and M67 parameterizations, respectively. Fitting procedure is described in text and Sections S4-S5. See Figure S1 for error bars. Experimental clustering is tighter in the 1-parameter case. Because the data contain insufficient information to determine two parameters independently, fit degeneracy in the 2-parameter case produces strong correlation between derived values for the equilibrium fractionation factor α_{eq} and the isotopic composition of wall outgassing R_w.

S3 Isotopic model for expansion experiments

We model the evolving isotopic composition in the vapour during a pseudo-adiabatic expansion experiment from the conservation of mass mixing ratio of the heavier isotopologue of the total water content inside AIDA, given a sink due to ice deposition and a source from wall outgassing during pumpdowns. Ice deposition is assumed to proceed with an unknown fractionation factor α_{eff} that is dependent on both temperature and saturation: $\alpha_{\text{eff}} = \alpha_k \alpha_{\text{eq}}$, where α_{eq} is the temperature-dependent equilibrium fractionation factor and α_k the kinetic modification. The isotopic composition of the wall contribution is an unknown R_w, fit either as a free parameter or as a function of α_{eq} (See 4.2).

We denote the mass mixing ratio of vapour and ice phases as r_v and r_i (and those of the heavy isotoplogue as r'_v and r'_i; we use the prime symbol throughout to denote the isotopically substituted quantity). The isotopic ratios for vapour and ice are then $R_v = r'_v/r_v$ and $R_i = r'_i/r_i$, respectively.

Conservation of mass of the abundant isotopologue can be written simply as:

$$\frac{dr_v}{dt} = -P_{\text{vi}} + S_{\text{wv}}, \tag{1}$$

$$\frac{dr_i}{dt} = P_{\text{vi}}, \tag{2}$$

where P_{vi} and S_{wv} stand for the depositional production of ice from vapour and the source of vapour from wall outgassing, respectively. (Both are > 0 in normal conditions.) The mixing ratio of total water r_{tot} (vapour plus ice) in the chamber then evolves as $dr_{\text{tot}}/dt = S_{\text{wv}}$. The wall contribution can be assumed to be directly into the vapour phase.

Conservation of the heavy isotopologue content gives:

$$\frac{dr'_v}{dt} = -\alpha_{\text{eff}} R_v P_{\text{vi}} + R_w S_{\text{wv}}, \tag{3}$$

where R_v and R_w are the isotopic ratios of chamber vapour (measured) and of vapour outgassing from the wall (unknown). The first term on the right-hand side of Eq. (3) describes the tendency of the vapour during depositional growth of ice. The isotopic ratio of the surface of an ice crystal growing by deposition is $R_i^{(s)} = \alpha_{\text{eff}} R_v$, where α_{eff} is the temperature- and saturation-dependent effective fractionation factor [25]. α_{eff} differs from α_{eq} when diffusion-limited growth produces kinetic fractionation between the vapour and the ice surface.

Expanding Eq. (3) using the definition of R_v and substituting into Eq. (1) yields the model for the evolution of vapour isotopic ratio in the chamber during the pumpdown:

$$\boxed{\frac{dR_v}{dt} = -\left(\alpha_{\text{eff}} - 1\right) R_v \frac{P_{\text{vi}}}{r_v} + \left(\gamma - 1\right) R_v \frac{S_{\text{wv}}}{r_v}.} \tag{4}$$

where $\gamma \equiv R_w/R_v$. The first term on the RHS describes distillation due to ice depositing during the pumpdown, and the second term describes enrichment due to wall outgassing. γ plays a role symmetric to α_{eff}, i.e. it describes the enrichment of outgassing vapour relative to that of chamber vapour. In the limit that $R_w \to R_v$, Eq. (4) reduces to the equation for simple Rayleigh distillation.

In a few experiments, we find that $S_{\mathrm{wv}} < 0$, i.e. total water mixing ratio decreases for short periods. Such cases would correspond to situations where the walls are not outgassing, but rather ice is depositing both on chamber walls and on crystals inside the chamber. In these instances we modify the model in Eq. (4) by reassigning variables as follows:

$$-P_{\mathrm{vi}} \rightarrow -P_{\mathrm{vi}} + S_{\mathrm{wv}}, \tag{5}$$

$$S_{\mathrm{wv}} \rightarrow 0. \tag{6}$$

In the experiments described here, isotopic doping does not affect retrieval of the equilibrium fractionation factor. Because doping levels are only ∼10-20 times natural abundance, the heavier isotopologue is still dilute with respect to the lighter isotopologue. In the dilute case, by Raoult's Law, the equilibrium fractionation factor will be equal to the ratio of HDO to H_2O partial pressures over pure HDO and H_2O, respectively.

The kinetic modification of the fractionation factor can be significant in some experiments, particularly those at cold temperatures and high supersaturation with respect to ice. We model the kinetic fractionation factor as linked to the equilibrium factor at ice deposition by the relationship:

$$\alpha_k = \frac{S_i}{\alpha_{\mathrm{eq}} \cdot g\,(S_i - 1) + 1} \tag{7}$$

where g is a coefficient that controls the magnitude of kinetic modifications. In the standard diffusive model of [25], g is equal to the ratio of molecular diffusivities of H_2O and HDO ($g = \mathrm{d} = D_v/D'_v$). In a variation of the model that includes surface kinetic effects, g is a more complex term that is a function of not only d but ice crystal diameter, thermal velocities, and the ratio of deposition coefficients for H_2O and HDO [26]. This model is discussed in detail in S6. In all analyses here, we omit effects related to the ratio of ventilation coefficients (negligible for small crystals and low temperatures, see [25, 27]), thermal impedance (effects on α_{eq} of order 10^{-3} or less), and corrections due to variation of thermodynamic quantities across the thermal boundary layer (small in all cases, see [28]).

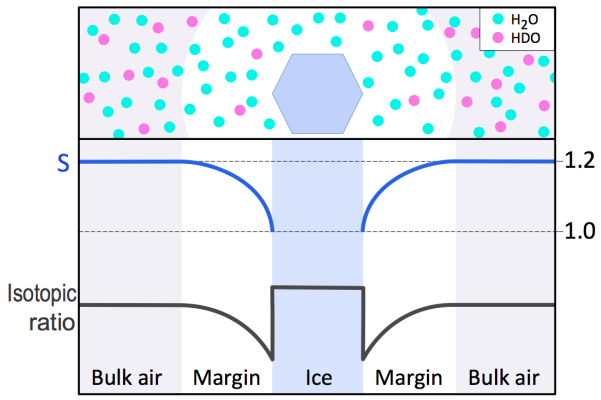

Figure S6: Cartoon demonstrating the effects of diffusion limitation on isotopic fractionation during ice growth. When diffusion becomes limiting, the effective fractionation becomes lower than in the equilibrium case because vapour isotopic composition is lower in the near field than in the bulk gas. This isotopic gradient arises primarily through two mechanisms: preferential uptake of the heavier isotopologue (α_{eq}) and lower diffusivity of the heavier isotopologue (d). In more complex models, differences in deposition coefficients between isotopologues can also play a role. See S6 for further discussion.

S4 Fitting protocol: individual experiments

S4.1 Region selection

To determine the isotopic fractionation factor, it is important to select a region of the experiment where the deposition of vapour as ice is maximal and the wall contribution is minimal, since the isotopic composition of the wall contribution is an unknown that we are approximating as constant. Most ice growth occurs in the first few minutes of each experiment, while outgassing from the chamber walls becomes progressively more important as the experiment proceeds. Restricting the analyzed region to a segment near the beginning of each experiment therefore maximizes signal from the isotopic fractionation and minimizes contributions from the wall: the two terms on the right side of Eq. (4). For each experiment (defined as beginning at the onset of pumping) we select the analysis region using the criteria:
Beginning

- At least 2% of the initial vapour must have deposited as ice
- The isotopic ratio must have changed by at least 0.5% of its initial value

End

- The outgassing rate must be less than or equal to the ice deposition rate
- The cumulative flux from the chamber walls must be less than 15% of the initial vapour

Regions selected based on these criteria range from 54 to 223 seconds long, with a mean length of 136 seconds. Region start times begin between 30 and 200 seconds after the onset of pumping, so that the analysis region does not include the first several degrees of cooling. Start times are later at the coldest temperatures because of higher nucleation thresholds and slower rates of ice growth.

S4.2 Model implementation

The fractionation factors are estimated for each pumpdown by minimizing the difference between observed and modeled vapour isotopic ratios, with the isotopic ratios modeled according to Eq. (4). To arrive at a closed form solution, we parametrize α_{eq} and γ as follows:

- **equilibrium fractionation factor:** $\alpha_{\mathrm{eq}} = \alpha_0 + \left.\frac{\partial \alpha_{\mathrm{eq}}}{\partial T}\right|_0 (T - T_0)$, where T_0 is the temperature at the beginning of the pumpdown. This linearization is acceptable because the variation in α_{eq} over the course of each pumpdown is expected to be a small fraction of the dynamic range of α_{eq} over all pumpdowns. Temperature changes during pumpdowns are of order 5-9 K (2-5 K for regions analyzed), producing change in α_{eq} of less than $\sim 5\%$). This parameterization introduces a dependence of α_{eq} on the unknown $\frac{\partial \alpha_{\mathrm{eq}}}{\partial T}$ and so mandates an iterative solution: we start from an initial guess of $\frac{\partial \alpha_{\mathrm{eq}}}{\partial T}$, solve for α_0 in individual experiments, fit for the global temperature dependence, update $\frac{\partial \alpha_{\mathrm{eq}}}{\partial T}$ based on that solution, and iterate to convergence.

- **relative isotopic enrichment of outgassing vapour:** $\gamma = R_w/R_v$, with R_v the measured vapour isotopic composition, and R_w the isotopic composition of wall outgassing assumed constant during the analyzed period of each experiment. In reality the composition of the ice layers coating the chamber walls may show some structure, but the outgassing composition likely varies sufficiently slowly to justify its approximation as constant. We set the constant R_w in two ways:
  - **2-parameter fit:** We fit R_w as a free parameter independent from α_{eq}. In practice, the pumpdowns do not contain sufficient information to fully constrain R_w and α_{eq} separately, and the fitted values of the two variables are correlated. We use this fit as a reality check on results, and to estimate error bars on α_{eq} for individual experiments.
  - **1-parameter fit:** $R_w = \alpha_{\mathrm{eq}} \cdot R_{v0}$. We assume the wall outgassing composition is that of an ice layer in equilibrium with chamber vapour before the pumpdown. R_w is then tied to the equilibrium fractionation factor α_{eq} and the measured pre-pumpdown isotopic ratio in chamber vapour R_{v0}. Data points in manuscript Figure 2 and stated coefficients for α_{eq} are taken from this fit.

Treatment of other model variables. While we fit on the raw 1-second measurements of isotopic ratio, we use an effectively smoothed version of the measured evolving water vapour and total water to compute the terms P_{vi}/r_v and S_{wv}/r_v in Eq. (4). That is, we take the low-order trend by computing the lowest SSA eigenmodes of the relevant measured time series ([29], see S4.4 for further discussion of SSA method). The modeled evolution of the isotopic ratio of vapour in the chamber is then determined by integrating Eq. (4) using a Runge-Kutta method with adaptative stepsize control, and the modeled isotopic ratio is fit to the raw measured isotopic ratio as described in the next section.

S4.3 Parameter and uncertainty estimation

We estimate parameters by the method of maximum likelihood. We denote the vector of parameters to estimate as $\boldsymbol{\theta}$. In the 2-parameter fit, $\boldsymbol{\theta} = [\theta_1,\, \theta_2]^T$ with $\theta_1 = \alpha_0$ and $\theta_2 = \gamma_0$. In the 1-parameter fit, $\boldsymbol{\theta} = [\theta_1]$ with $\theta_1 = \alpha_0$.

Measured and modeled isotopic ratios are related as follows:

$$\mathbf{R}^{\mathrm{obs}} = \mathbf{R}^{\mathrm{m}}(\boldsymbol{\theta}) + \boldsymbol{\varepsilon} \tag{8}$$

where $\mathbf{R}^{\mathrm{obs}}$ are measured and $\mathbf{R}^{\mathrm{m}}$ modeled isotopic ratios and $\boldsymbol{\varepsilon}$ are inferred measurement errors, discussed in S4.4. Because the errors are reasonably independent and normally distributed, the likelihood of $\boldsymbol{\theta}$ (that is, the probability of observing $\mathbf{R}^{\mathrm{obs}}$ given $\boldsymbol{\theta}$) can be written as:

$$\begin{aligned} L(\boldsymbol{\theta}) &= p\left(\mathbf{R}^{\mathrm{obs}}|\boldsymbol{\theta}\right) \\ &= \frac{1}{(2\pi)^{\frac{N}{2}}\sqrt{\det(\mathbf{C}_{\boldsymbol{\varepsilon}})}} \\ &\quad \times \exp\left[-\frac{1}{2}\left(\mathbf{R}^{\mathrm{obs}} - \mathbf{R}^{\mathrm{m}}(\boldsymbol{\theta})\right)^T \mathbf{C}_{\boldsymbol{\varepsilon}}^{-1}\left(\mathbf{R}^{\mathrm{obs}} - \mathbf{R}^{\mathrm{m}}(\boldsymbol{\theta})\right)\right] \end{aligned} \tag{9}$$

where N is the dimension of $\mathbf{R}^{\mathrm{obs}}$ (or $\mathbf{R}^{\mathrm{m}}$) and $\mathbf{C}_{\boldsymbol{\varepsilon}} = \mathrm{E}\left[\boldsymbol{\varepsilon}\boldsymbol{\varepsilon}^T\right] = \mathrm{diag}\left(\sigma_i^2\right)$ is the covariance matrix of measurement errors. (See S4.4 for discussion of estimating measurement error σ_i.) The maximum likelihood estimator of $\boldsymbol{\theta}$ is then the value $\hat{\boldsymbol{\theta}}$ that maximizes $L\left(\boldsymbol{\theta}\right)$. (We use the "hat" symbol throughout to denote an estimated quantity.) In practice, we minimize $-\mathcal{L}\left(\boldsymbol{\theta}\right) = -\log L\left(\boldsymbol{\theta}\right)$, which is equivalent to minimizing the following quantity:

$$\frac{1}{2}\sum_{i=1}^{N}\left(\frac{R_i^{\mathrm{obs}} - R_i^{\mathrm{m}}\left(\boldsymbol{\theta}\right)}{\sigma_i}\right)^2 \tag{10}$$

The minimization of $-\mathcal{L}\left(\boldsymbol{\theta}\right)$ is carried out using a quasi-Newton algorithm.

Uncertainty in retrieved parameters $\boldsymbol{\theta}$ is estimated using Fisher matrix theory. The likelihood $L\left(\boldsymbol{\theta}\right)$ is asymptotically Gaussian near its maximum, i.e. it can be written:

$$L\left(\boldsymbol{\theta}\right) \propto \exp\left[-\frac{1}{2}\left(\boldsymbol{\theta} - \hat{\boldsymbol{\theta}}\right)^T \mathbf{C}_{\boldsymbol{\theta}}^{-1}\left(\boldsymbol{\theta} - \hat{\boldsymbol{\theta}}\right)\right] \tag{11}$$

where $\mathbf{C}_{\boldsymbol{\theta}}$ is the covariance matrix of the estimated parameters. (The inverse of $\mathbf{C}_{\boldsymbol{\theta}}$ is called the Fisher information matrix.) $\mathbf{C}_{\boldsymbol{\theta}}$ is computed as the inverse of the Hessian of the log-likelihood:

$$\mathbf{C}_{\boldsymbol{\theta}} = -\left(\nabla_{\boldsymbol{\theta}\boldsymbol{\theta}}\mathcal{L}\right)^{-1} = -\left(\nabla_{\boldsymbol{\theta}\boldsymbol{\theta}}\log L\right)^{-1} \tag{12}$$

(The Hessian matrix is computed using centered finite differences.) The diagonal of $\mathbf{C}_{\boldsymbol{\theta}}$ then contains the variance estimates of the parameters θ_i. That is, $\mathbf{C}_{\boldsymbol{\theta}}$ produces an estimate of the uncertainty σ_n^{α} in each retrieval of an equilibrium fractionation factor $\hat{\alpha}_n$. These uncertainties are shown as the 2σ error bars in Figure S1 and manuscript Figure 4.

Comparison of the estimated σ_n^{α} for individual experiments and the distribution of derived fractionation factors $\hat{\alpha}_n$ around the fit to all experiments suggests that these error estimates are appropriate for the low-temperature experiments, in which signal-to-noise is the dominant factor driving uncertainty, but are underestimates for the warmer experiments (T> 210 K), in which un-modeled systematic errors (likely driven by chamber inhomogeneities) dominate. We do not attempt to estimate additional contributions to experimental error, but note that true uncertainties may be a factor of three larger at the warmer end of the experimental temperature range.

S4.4 Measurement error estimation

The likelihood function used to estimate parameters for each pumpdown (Eq. 10) requires an estimation of the intrinsic uncertainty σ_i in the isotopic ratio measurements. Determining this uncertainty would be trivial if its only source were measurement precision and instrument characteristics were fixed; in this case measurement errors could simply be estimated from instrument performance in static conditions. Error estimation during pumpdowns is more challenging because instrument performance can be altered by vibrations and attenuation of signal, and because chamber inhomogeneities increase during pumpdowns. Effective measurement errors are therefore not constant during experiments. Since we are interested in changes in isotopic ratio rather than absolute changes in concentrations, uncertainties in spectroscopic parameters and most other factors affecting accuracy do not affect results.

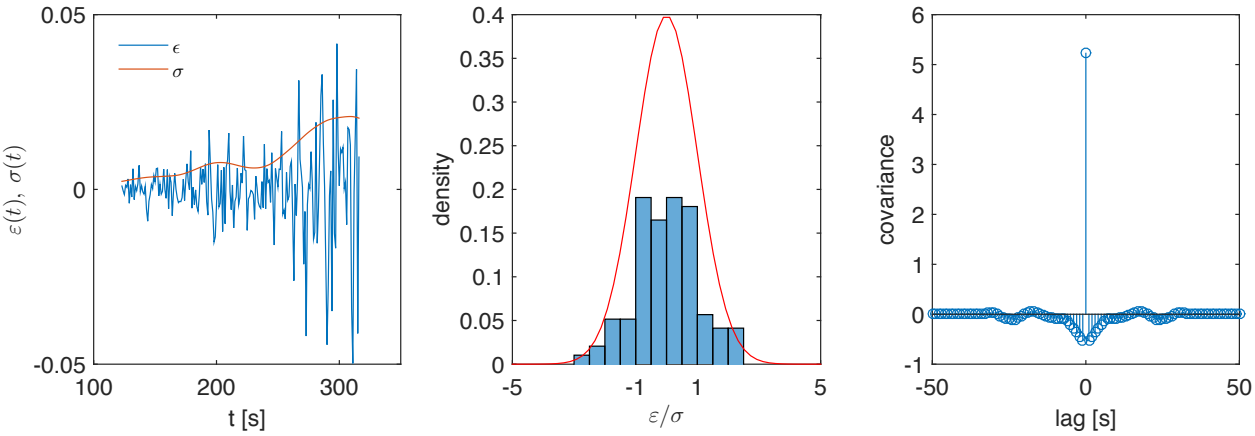

Figure S7: Example of estimated noise on isotopic ratio measurements for experiment #6. **Left:** The reconstructed noise from the trailing SSA eigenmodes and their associated standard deviation. Note that noise grows over the course of the pumpdown. **Center:** The standardized error is reasonably normally distributed. **Right:** The reconstructed noise is reasonably decorrellated in time.

To estimate effective measurement error in a timeseries of isotopic ratio measurements, we assume that the effective error is manifested as deviations from a smoothly evolving isotopic ratio. While the fit for $\hat{\alpha}_n$ is performed on raw isotopic measurements, we estimate errors by taking a Singular Spectrum Analysis (SSA) [29] on that raw timeseries. SSA decomposes the timeseries into a sum of eigenmodes (temporal principal components), each of them accounting in decreasing order for a fraction of the variance of the original time series. We use the first few leading eigenmodes to construct the assumed smoothly evolving timeseries, and consider the trailing eigenmodes to represent the noise ε_i on the measured isotopic ratio. The rank at which we set this eigenmode separation is determined by the test that errors must be reasonably time-decorrelated.

Note that this method cannot distinguish one important experimental artifact: low-frequency fluctuations due to chamber inhomogeneities, which are correlated in time. Isotopic measurements probe only the volume intersected by our infrared laser beam; chamber air circulating across the beam path results in small but important real fluctuations in temperature, water vapour content, and ice crystal number density, with timescale ~ 30 s.

Because effective noise characteristics change during a pumpdown (Fig. S7, left), we cannot simply take measurement uncertainty as the sample standard deviation of the noise ε_i, but instead must construct a standard error σ_i that changes over the i datapoints of the pumpdown. For this estimation, we use the fact that the noise covariance matrix $\mathrm{E}\left[\boldsymbol{\varepsilon}\boldsymbol{\varepsilon}^T\right] = \mathrm{diag}\left(\sigma_i^2\right)$, so that σ_i^2 can be taken as the leading SSA eigenmode of the ε_i^2 time series.

We then test the validity of our approach for estimating ε_i and associated standard deviation σ_i by checking the distribution of the standardized errors ε_i/σ_i in each pumpdown. Because our approach models the likelihood of our parameters as a multivariate normal distribution of variance σ_i, values of ε_i/σ_i during a pumpdown should be normally distributed with variance 1 and decorrelated in time. We find that they are indeed sufficiently well behaved with respect to our basic assumptions (Fig. S7). In the next section, we find that the σ_i are also optimal, in the sense that rescaling only marginally improves likelihoods.

S4.4.1 Error rescaling

As a check on our error estimation procedure, we also test the possibility that the covariance matrix of measurement errors $\mathbf{C}_{\boldsymbol{\varepsilon}}$ previously derived is known only up to a scaling factor. That is, we consider whether the standard deviations of measurement errors may in fact be $s\sigma_i$, where s is a global scaling factor attached to each pumpdown. In that case, $\mathbf{C}_{\boldsymbol{\varepsilon}}$ would be known up to s^2. In the previous section, we assumed $s = 1$. We now determine s by treating it as one of the parameters estimated by maximizing the likelihood function. For instance, with $\theta_1 = \alpha_0$ and $\theta_2 = \gamma_0$, we set $\theta_3 = s$. The minimization of $-\boldsymbol{\mathcal{L}}(\boldsymbol{\theta}) = -\log L(\boldsymbol{\theta})$ is now equivalent to minimizing the quantity:

$$\sum_{i=1}^{N} \log(\theta_3 \sigma_i) + \frac{1}{2} \sum_{i=1}^{N} \left(\frac{R_i^{\mathrm{obs}} - R_i^{\mathrm{m}}(\theta_1, \theta_2)}{\theta_3 \sigma_i} \right)^2 . \tag{13}$$

As can be seen in Fig. S8, rescaling the errors improves the likelihood only marginally, meaning this operation is essentially superfluous for estimating the fractionation factors and their associated standard errors. These results imply that the characterization of errors described in Sec. S4.4 is already nearly optimal and cannot be much improved.

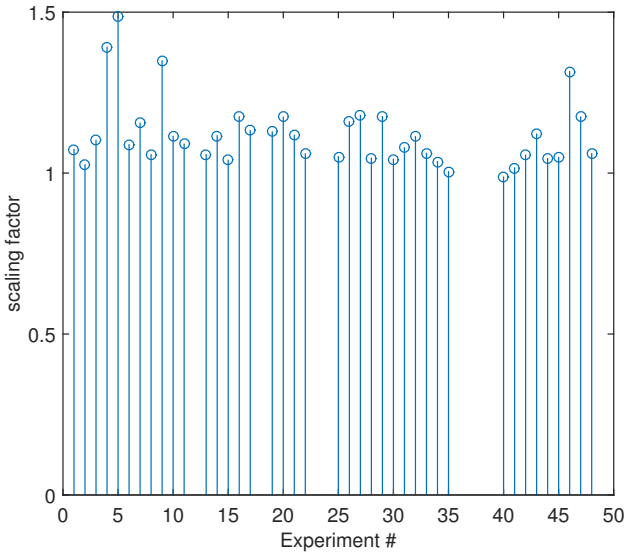

Figure S8: The derived scaling factor s for error for all experiments fits to close to 1, demonstrating that the noise reconstruction from the SSA eigenmodes provides a good estimation of the covariance matrix of measurement errors (likelihood is only marginally improved by rescaling). This means that the uncertainty on α_0 for individual pumpdowns is sufficiently well-estimated using the minimization of the likelihood function without the inclusion of an additional scaling factor.

S5 Fitting protocol: temperature dependence

S5.1 Global fit procedure

After repeating the estimation procedure described above (S4.3) for all n experiments to obtain individual estimates for the fractionation factors $\hat{\alpha}_n$ at temperatures T_n, and corre-

sponding uncertainties σ_n^α, we then fit for the temperature dependence of α_{eq}, assuming that it follows the form:

$$\log \alpha_{\text{eq}} = a_0 + \frac{a_1}{T^2} \tag{14}$$

A $1/T^2$ temperature dependence was also assumed in the M67 parameterization [4].

Eq. 14 stems from quantum mechanical considerations [2, 30], and is derived by expanding the partition functions for isotopically substituted and non-substituted species under the harmonic approximation for the force field potentials. A more general form including the effects of anharmonicity would be:

$$\log \alpha_{\text{eq}} = \delta_0 + \frac{\delta_1}{T} + \frac{\delta_2}{T^2} \tag{15}$$

In most isotopic systems, the anharmonic term δ_1/T can be neglected at high temperatures [31], but in the case of hydrogen partitioning the effects of anharmonicity and non-classical rotation are important. It is not straightforward to determine the appropriate functional form for the isotopic fractionation factor for HDO to H_2O, but our measurements suggest that Eq. (14) sufficiently represents the functional relationship, since the experimentally derived values for the fractionation factor for individual pumpdowns appear roughly linear in $\log(\alpha_{\text{eq}})$ vs. $1/T^2$ space.

To provide consistency with previously measured values for the fractionation factor at higher temperatures, which agree well, we further impose the constraint that we take the highest temperature measurement from [4] to be a true value, fixing $\alpha_0 = 1.143$ at $T_0 = -6$ °C. This constraint does not significantly affect the parameterization of α_{eq} over our experimental temperature range.

To estimate the temperature dependence, we make Eq. (14) linear with a change of variables to $x = \log \alpha_{\text{eq}}$ and $t = 1/T^2$: $x = a_0 + a_1 t$.

Including the constraint at T_0 then yields:

$$x - x_0 = a_1 (t - t_0) \tag{16}$$

and estimating the temperature dependence δ_1 becomes a linear estimation problem:

$$\mathbf{x} - \mathbf{x_0} = \mathbf{H} \cdot a_1 + \mathbf{w} \tag{17}$$

where $\mathbf{x} - \mathbf{x_0}$ describes fractionation values derived for individual experiments: $\mathbf{x} - \mathbf{x_0} = [0, x_1 - x_0, ..., x_N - x_0]^T$, and $\mathbf{H}$ the experimental temperatures: $\mathbf{H} = [0, t_1 - t_0, ..., t_N - t_0]^T$. $\mathbf{w}$ is the vector of errors on the determination of $\log \alpha_{\text{eq}}$; the covariance matrix of $\mathbf{w}$ is $\mathbf{C_w} = \text{diag}\left[(\sigma_n^\alpha / \hat{\alpha}_n)^2\right]$. (See S4.3 for discussion of $\hat{\alpha}_n$ and σ_n^α.) Following standard theory, the best linear estimator of a_1 is:

$$\hat{a}_1 = \left(\mathbf{H}^T \mathbf{C}_{\text{w}}^{-1} \mathbf{H}\right)^{-1} \mathbf{H}^T \mathbf{C}_{\text{w}}^{-1} \cdot (\mathbf{x} - \mathbf{x_0}) \tag{18}$$

and its uncertainty is $(\sigma^{a_1})^2 = \left(\mathbf{H}^T \mathbf{C}_{\text{w}}^{-1} \mathbf{H}\right)^{-1}$, which can be used to build confidence intervals.

Note that during the estimation procedure, $\mathbf{C}_{\text{w}}$ is internally resized in order to better match the dispersion of the residuals. That is, $\mathbf{C}_{\text{w}}$ is rescaled by a factor such that the variance of the standardized residuals becomes 1 (compensating for the underestimation of uncertainties for individual experiments noted earlier).

This rescaling does not affect the estimated $\hat{a}_1$ but increases its estimated uncertainty $(\sigma^{a_1})^2$ by approximately a factor of three. The confidence intervals on $\alpha_{\rm eq}$ shown throughout this work reflect this conservative estimate. The uniform rescaling is inappropriate given that uncertainties appear underestimated only for the warmer experiments, but sensitivity tests show that the resulting parametrization for $\alpha_{\rm eq}$ is negligibly affected by the weighting of individual experiments. (See S7.3.)

S5.2 Results for different treatment of R_w

Different assumptions about the isotopic composition R_w of the wall outgassing flux produce different estimates of equilibrium fractionation $\hat{\alpha}_n$ for individual experiments, which in turn can lead to slightly different inferred temperature dependence for $\alpha_{\rm eq}$. (See Fig. S5.) As described in S4.2, we use two different methods of fitting, each with desirable and undesirable features.

- In the 1-parameter case, we treat the wall as ice that has equilibrated with initial chamber vapour, ie. $\gamma = \alpha_{\rm eq} R_{v0}^{obs}$. The only retrieved parameter is then the fractionation factor (α_0). In this case, the estimated uncertainties on α_0 for all experiments are implausibly optimistic, since the error bars reflect only measurement errors.

- In the 2-parameter case, we treat the isotopic composition of the wall outgassing flux R_w (and so $\gamma = R_w/R_v^{obs}$) as an unknown that must be fit. Error bars in this case are considerably larger, reflecting additional uncertainty in γ. (The off-diagonal terms of the Fisher matrix are non-zero, indicating that the parameter determination errors for γ and α_0 are correlated.) The resulting uncertainty estimates σ_n^α arguably more closely approximate the true uncertainties on a determination of the fractionation factor. However, the dependence of the two parameters also produces fit degeneracy, with in many cases unphysically high values for R_w and correspondingly large α_0.

In this analysis we choose the 1-parameter fit as the default case, but make the further assumption that the uncertainty derived from the 2-parameter fit more closely approximates actual measurement uncertainty. Each choice produces a slightly different temperature dependence for $\alpha_{\rm eq}$, given in Table S4 below.

#	Assumption	a_0	a_1
(A)	2 parameter ($\theta_1 = \alpha_0,\ \theta_2 = \gamma_0$)	-0.0619	13959
(B)	1 parameter ($\theta_1 = \alpha_0,\ \sigma_n^\alpha$ from (A))	-0.0559	13525
(C)	1 parameter ($\theta_1 = \alpha_0$)	-0.0536	13364
(M67)	Merlivat and Nief, 1967	-0.0945	16289

Table S4: Parameters a_0 and a_1 obtained upon fitting $\log\alpha = a_0 + a_1/T^2$ to fractionation factors derived under various model assumptions, with M67 shown for comparison. Case (B) is that presented in the manuscript and shown in black in figures; case (A) is shown in purple.

S6 Evaluation of kinetic models

Because the IsoCloud 4 experiments include a variety of mean supersaturations $\bar{S}_i$, conditions in which kinetic isotope effects should have differing influence, they allow testing the predictions of different models for the kinetic modification to fractionation. In all cases, we assume that kinetic isotopic effects can be represented by Eq. (7), i.e.:

$$\alpha_k = \frac{S_i}{\alpha_{\mathrm{eq}} \cdot g\,(S_i - 1) + 1}$$

We test the effect of different proposed values for the parameter g, which is a function of d, the ratio of diffusivities of H_2O and HDO, and, in some treatments, of surface effects including the ratio of deposition coefficients between isotopologues.

S6.1 Kinetic fractionation models

We test two different treatments of kinetic isotopic effects.

Diffusive flux model: The default representation of kinetic modifications to fractionation in this work is the diffusive model of Jouzel and Merlivat [25], i.e. Eq. (7) with

$$g = \mathrm{d}$$

Diffusive plus surface-kinetics model: Nelson [26] extends the diffusive flux model to include surface kinetic effects by setting

$$g = \mathrm{d} \cdot \frac{1 + z'}{1 + z}$$

where $z = Z_S/Z_V$ is the ratio of the surface impedance to the vapour impedance, and as before, we denote quantities associated with the heavier isotopologue with a prime. If we assume spherical geometry for ice crystals, this expression can be rewritten as

$$g = \frac{\mathrm{d}k + \mathrm{yx}}{1 + k}$$

where x is the ratio of deposition coefficients for H_2O and HDO (x=β/β') and y is their ratio of thermal velocities ($\sqrt{19/18}$). The coefficient $k \equiv rv\beta/\left(4D_v\right)$, where r is the ice crystal radius and v, β, and D_v are the thermal velocity, deposition coefficient, and diffusion coefficient in air, respectively, for the abundant isotopologue H_2O. We make the simplifying assumption that $\beta = 1$; the value is unknown but is likely of order 1 [32]. We take the temperature- and pressure-dependent D_v from Hall and Pruppacher 1976 [33]. In the limit $k >> 1$, the expression reduces to that of the diffusive model. In the experiments analyzed here, values for k range from 2-15 across pumpdowns, essentially following the mean ice crystal diameter (2-14 μm). The greatest sensitivity to surface effects therefore occurs at the lowest temperatures, where ice crystal size and k are smallest. The ratio of deposition coefficients x is essentially unknown; Nelson [26] suggests that its value could plausibly lie between 0.8 and 1.2.

S6.2 Estimates of the isotopic diffusivity ratio

The value of d has been determined in a limited number of experiments, whose results are inconsistent within stated error bars. (Published values differ by as much as 3% while stated error bars are $< 0.1\%$.) We summarize published results below in Table S5. In this work we take as our default for d the value from Cappa et al. 2003 [34].

Kinetic isotope effects in our experiments are predominantly driven by equilibrium fractionation during ice deposition, with differences in diffusivity playing only a minor role. In the diffusive flux model for kinetic isotopic effects given above, d plays an identical role to the equilibrium fractionation factor α_{eq}: both appear only in the coefficient α_{eq}d, and while d is only a few percent above 1, α_{eq} is ∼1.2-1.4 over the experimental temperature range. Nevertheless, *uncertainty* in d can still contribute significantly to uncertainty in kinetic effects.

Measurement	**T (°C)**	**T (K)**	$\mathbf{D_{HDO}/D_{H_2O}}$	$\mathbf{D_{H_2O}/D_{HDO}}$ (d)
Ehhalt and Knott, 1965 [35]	20.0	293.2	0.9852 ± 0.003	1.0150
Cappa et al., 2003 [34]	20.0	293.2	0.9839	1.0164
Merlivat, 1978 [36]	21.0	294.2	0.9755 ± 0.0009	1.0251
Luz et al., 2009 [37]	*-83.2*	*190.0*	*0.9573*	*1.0446*
–	10.0	283.2	0.9720 ± 0.0005	1.0288
–	20.1	293.3	0.9775 ± 0.0005	1.0230
–	39.8	313.0	0.9798 ± 0.0005	1.0206
–	69.5	342.7	0.9841 ± 0.0003	1.0162

Table S5: Published estimates of the ratio of diffusivities for HDO and H_2O in air. Values from Cappa et al. are derived from kinetic theory and given without uncertainties. Values for Luz et al. in regular font are measurements; in italics is the value that would be extrapolated at 190 K by an unweighted linear fit to these values: d=1.0807-1.901·$10^{-4} \cdot T$, with T in Kelvin. (Only Luz et al. suggest a temperature dependence).

S6.3 Tests of kinetic models

We test the validity of models of the kinetic isotope effect by examining whether, after correction for kinetic contributions to fractionation, the values for equilibrium fractionation retrieved from individual experiments ($\hat{\alpha}_n$) show dependence on supersaturation S_i. A dependence on saturation would be interpreted as the signature of under- or over-correction for kinetic effects. Absence of a trend would suggest that the magnitude of kinetic effects had been correctly estimated.

Because the experiments analyzed here are conducted at different temperatures, and equilibrium fractionation is a function of temperature, we do not consider the derived equilibrium fractionation factors $\hat{\alpha}_n$ directly. Instead, we consider their implied coefficients $\hat{a}_1^n$. Because the model for α_{eq} is constrained to include a measured value at $T = -6°\text{C}$, our global fit for the temperature-dependent α_{eq} can be fully described by this single coefficient a_1. Similarly, each $\hat{\alpha}_n$ for an individual pumpdown defines a single $\hat{a}_1^n$ that quantifies the temperature dependence of the equilibrium fractionation factor that would be implied by

that experiment alone. In M67, a_1 is 16289. In our global fit, a_1 is slightly lower, 13525. If all measurements were perfect, and the equilibrium fractionation factor exactly followed the $1/T^2$ dependence of Eq. (14), then each experiment would produce $\hat{a_1}^n$ exactly equal to this a_1. In reality, values of $\hat{a}_1^n$ derived from individual experiments scatter around this value. (See cartoon in Fig. S9.)

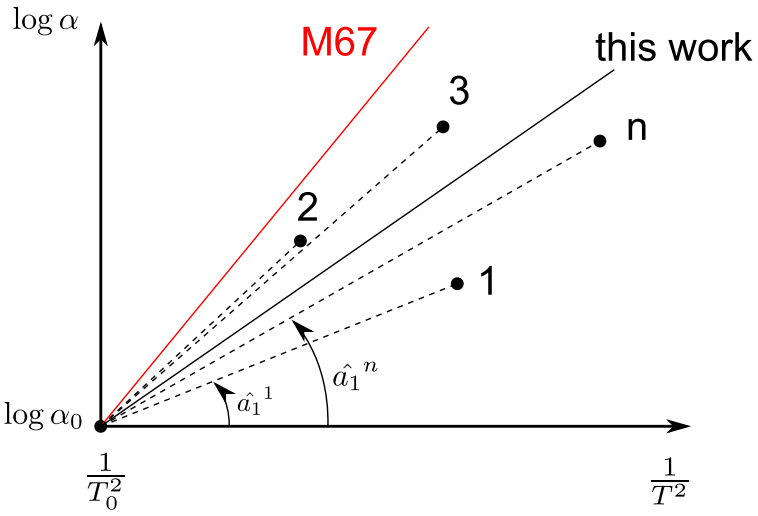

Figure S9: Cartoon to illustrate the slopes $\hat{a_1}^n$ that appear in manuscript Figure 5 and Figure S10. $\hat{a_1}^n$ is the slope in $\log\alpha$ vs. $1/T^2$ space of the line connecting the assumed constraint point $(1/T_0^2, \log(\alpha_0))$ with an experimentally derived point $(1/T^2, \log(\hat{\alpha}_n))$. Individual experiments in this work generally produce $\hat{a_1}^n$s (slopes of dashed lines) below that of M67 (solid red) and therefore produce a weaker temperature dependence for the globally fit α_{eq} (solid black).

Any over- or under-correction for kinetic effects would produce a systematic trend in the $\hat{a}_1^n$s with supersaturation S_i. If g in the kinetic model is incorrectly specified ($g \neq g_0$, where g_0 is the "true" value that would yield a perfect retrieval), then the resulting estimation of equilibrium fractionation α_{eq} would be biased, and that bias would depend on supersaturation:

$$\frac{\partial \alpha_{\mathrm{eq}}}{\partial S_i} = (g - g_0)\,\alpha_{\mathrm{eq}}^2 \tag{19}$$

This expression can be rewritten in terms of a_1 since

$$\ln \frac{\alpha_{\mathrm{eq}}}{\alpha_0} = a_1 \left(\frac{1}{T^2} - \frac{1}{T_0^2} \right) \tag{20}$$

Combining equations 19 and 20 shows that $\partial \ln a_1 / \partial S_i$ is directly linked to the choice of g:

$$\frac{\partial \ln a_1}{\partial S_i} = (g - g_0)\,\frac{\alpha_{\mathrm{eq}}}{\ln\left(\frac{\alpha_{\mathrm{eq}}}{\alpha_0}\right)}, \tag{21}$$

The absence of trend with S_i would therefore suggest that kinetic effects have been modeled correctly, i.e. $g = g_0$.

We conduct two tests to determine the validity of kinetic models and establish constraints on the parameters d and x. While we cannot constrain d and x simultaneously, we can examine their effects separately. First, we test a pure diffusive flux model (g = d) with different values of d. We fit for the optimal value of the diffusivity ratio d that eliminates supersaturation dependence, and determine bounds on potential values for d. We then test the diffusive-plus-surface-kinetic model with d set at the default value of Cappa et al. [34], and determine an optimum value and bounds for x given that assumption. That is, we assume that the value of the diffusivity ratio is known, and that any trend with saturation results from mis-estimation of surface kinetic effects due to an incorrect choice of the deposition coefficient ratio x. In both cases we fit for the trend of $\hat{a_1}^n$s vs. the deposition-weighted supersaturation

$$\bar{\mathrm{S}_i} = \int P_{vi} S_i / r_v dt / \int P_{vi} / r_v dt \tag{22}$$

assuming a linear relationship: $a_1\left(S_i\right) = m \cdot S_i + b$. We seek the value of g that yields zero slope ($m = 0$) by using a root-finding algorithm, and estimate bounds as described below. As in the fit for α_{eq}, we weight individual experiments by their uncertainty σ_n^{α} (See S4).

The results of these tests yield bounds on diffusivity and deposition coefficient ratios d and x that are consistent with literature estimates of their plausible ranges. Manuscript Figure 5 shows results of the test on d with the pure diffusive model. The implied optimal value of d=1.01 is slightly lower than any measurement, but with bounds of $\sim \pm 4\%$ spanning the published values in Table S5: $0.97 < \mathrm{d} < 1.05$. Figure S10 shows results of the test on x with the surface-kinetic model. Because the kinetic isotope effect is less sensitive to uncertainty in x, the test provides a looser constraint, with bounds on x exceeding $\pm 20\%$: $0.74 < \mathrm{x} < 1.17$, spanning the range of 0.8-1.2 suggested by Nelson [26]. The central value of x=0.96 would imply that HDO molecules were slightly more likely to be accommodated into the crystal lattice than H_2O, but results are also consistent with x=1.

The looseness of these constraints stems from the small sample size of those IsoCloud 4 experiments sensitive to kinetic isotope effects. Only six experiments have deposition-weighted supersaturations above 1.2, three of those at temperatures low enough that signal-to-noise is poor and uncertainty in isotopic ratio measurements high. The small sample size also means that individual outliers can strongly bias results. In this analysis, we omit experiments #4, 26, and 48, three outlier experiments whose small nominal error bars leave them inconsistent with the global derived α_{eq} to greater than 5-σ with respect to their estimated uncertainties; including these experiments would substantially alter the derived optimal values for d and x. Even assuming the uncertainties are underestimated by 3x, all three experiments remain outliers, with 2.5-σ residual with respect to their estimated errors. Each of these experiments are also outliers with respect to the distribution in their respective temperature groups. The small sample size means that for d and x, IsoCloud results should be considered suggestive rather than conclusive. These results do however confirm the validity of kinetic models, and serve as a proof of concept of the approach. Future experimental campaigns targeted at kinetic isotope effects should be able to provide stronger constraints.

To estimate bounds on kinetic isotope effect parameters, we evaluate uncertainty σ_g on estimating g_0 by propagating the uncertainty σ_{slp} on the slope $\partial \ln a_1 / \partial S_i$. Because experiments at different temperatures have different α_{eq}, we know that uncertainty only to

within some range. From Eq. (21), σ_g must lie in the range:

$$\sigma_{\rm slp} \cdot \min\{\frac{\ln\left(\frac{\alpha_{\rm eq}}{\alpha_0}\right)}{\alpha_{\rm eq}}\} \leq \sigma_g \leq \sigma_{\rm slp} \cdot \max\{\frac{\ln\left(\frac{\alpha_{\rm eq}}{\alpha_0}\right)}{\alpha_{\rm eq}}\} \tag{23}$$

where the min and max values are over all experiments in the analysis. When assuming the diffusive model with $g =$d to obtain constraints on d, we conservatively take the upper limit as the estimated uncertainty in d. When testing the surface-effect model with $g = (\mathrm{d}k + \mathrm{yx}) / (1 + k)$, to obtain constraints on x, we can rewrite Eq. (21) as:

$$\frac{\partial \ln a_1}{\partial S_i} = (\mathrm{x} - \mathrm{x}_0) \frac{y}{1+k} \frac{\alpha_{\rm eq}}{\ln\left(\frac{\alpha_{\rm eq}}{\alpha_0}\right)} \tag{24}$$

where x_0 is the value of x that would yield the "true" retrieval of $\alpha_{\rm eq}$. The uncertainty σ_x on x_0 then satisfies the relationship:

$$\sigma_{\rm slp} \cdot \min\{\frac{1+k}{y} \frac{\ln\left(\frac{\alpha_{\rm eq}}{\alpha_0}\right)}{\alpha_{\rm eq}}\} \leq \sigma_x \leq \sigma_{\rm slp} \cdot \max\{\frac{1+k}{y} \frac{\ln\left(\frac{\alpha_{\rm eq}}{\alpha_0}\right)}{\alpha_{\rm eq}}\}\,, \tag{25}$$

We again conservatively take the upper limit as our estimate of uncertainty in x_0.

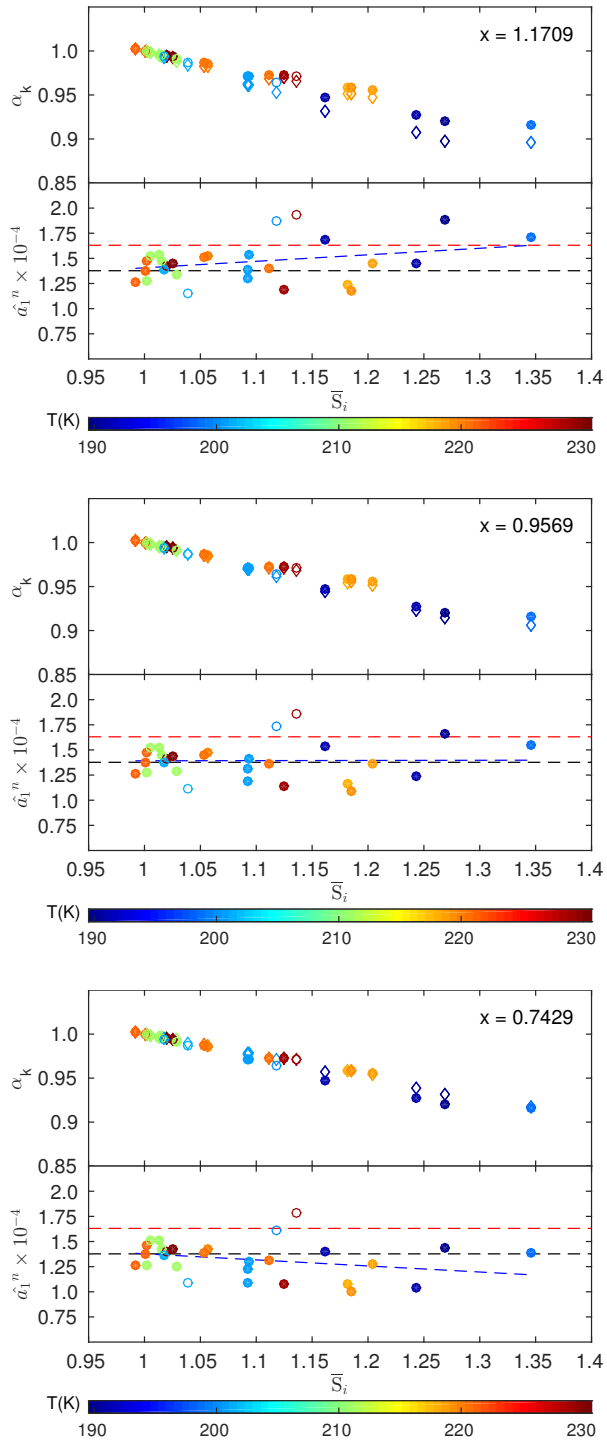

Figure S10: Effect of choice of x (ratio of isotopic deposition coefficients) on calculated kinetic and retrieved equilibrium fractionation in experiments, plotted against deposition-weighted supersaturation. Top halves of panels show kinetic effects from the diffusive/surface-kinetic model of [26] with a given value of x (circles), and with the diffusive model of [25] (open diamonds) for reference. In all cases d is set at 1.0164, the default value from Cappa et al. Bottom halves shows resulting equilibrium fractionations as computed slopes $\hat{a}_1^n$. (See Fig. S9.) Deviation from slope 0 implies a mis-specified kinetic model. Dashed lines show a_1 values corresponding to M67 (red) and this work (black). Blue line is weighted fit to $\hat{a}_1^n$s, excluding three outlier experiments (#4, 26, and 48, shown as open circles). The three panels show the fitted optimal value for x and conservative upper and lower bounds. Bounds span suggested range of plausible values for x.

S7 Sensitivity tests on determination of $\alpha_{\mathbf{eq}}$

We perform several tests to evaluate the robustness of our determination of α_{eq}. We test for sensitivity to model assumptions (values for d), to measurement uncertainties (experimental region selection and bias in measured H_2O), and to fitting procedure (weighting of experiments in global fit). All factors produce relatively minor changes, and retain the finding of α_{eq} below M67.

S7.1 Sensitivity to region choice

In all analyses described previously, we choose the experimental region analyzed for each pumpdown by a set of fixed criteria, described in S4:

- that ice deposition rate exceeds wall outgassing: $\epsilon = S_{wv}/P_{vi} < 1$
- that cumulative ice deposition exceeds a fraction Γ of initial vapour, with $\Gamma = .02$
- that the isotopic ratio has dropped by a fraction Δ from its initial value, with $\Delta = 0.005$

The choice of region length can affect derived values of equilibrium fractionation for individual experiments ($\hat{\alpha}_n$) and therefore global fits for α_{eq}, for several reasons. As discussed previously, wall outgassing isotopic composition is assumed constant but may show some trend over time. More importantly, chamber inhomogeneities produce fluctuations in measured quantities with timescales ∼30 s. With our region selection criteria, the timeseries analyzed for each pumpdown may contain 2-8 cycles of statistically significant fluctuations in measured quantities that affect $\hat{\alpha}_n$. Default values for ϵ, Γ, and Δ were chosen such that derived values for $\hat{\alpha}_n$ are relatively stable to moderate extensions or reductions of region length. We evaluate here sensitivity to these parameter choices by performing a Bayesian analysis. We allow ϵ, Γ, and Δ to vary arbitrarily (within bounds $\epsilon \in [0.3, 2.0]$, $\Gamma \in [0.01, 0.05]$ and $\Delta \in [0.001, 0.01]$), producing a wide range of candidate time segments. (In this analysis the region choice is randomly chosen and all experiments are evaluated with the same choice of parameters to define the region length.) We use each choice to derive an estimate for α_{eq}, and examine all results that meet goodness-of-fit criteria.[1] Details of the analysis are described at the end of this section.

While the region choice parameters can strongly affect a resulting global fit for α_{eq}, we find that the central value of the distribution of estimated $\hat{a}_1$ in this analysis is very close to that derived with the region choice algorithm of S4. That is, the most probable temperature-dependent α_{eq} in the Bayesian analysis is consistent with the determination of α_{eq} in our previous analyses (Fig. S11). (The confidence interval derived from the Bayesian analysis

[1] **Goodness of fit:** We evaluate the goodness of the fit by: first, checking that the minimizer has converged to a solution ($\nabla_{\boldsymbol{\theta}}\mathcal{L} \approx \mathbf{0}$ to specified tolerance and $\nabla_{\boldsymbol{\theta}\boldsymbol{\theta}}\mathcal{L}$ positive definite); second, inspecting the normalized residuals

$$\frac{R_i^{\mathrm{obs}} - R_i^{\mathrm{m}}(\boldsymbol{\theta})}{\sigma_i}$$

and checking that their distribution does not significantly deviate from a Gaussian with mean 0 and variance 1 (to ensure compliance with Eq. (11)). This is assessed by a Kolmogorov-Smirnov test with a 5% significance level. Only fits to the randomly chosen regions which pass the goodness of fit test are included in the probability distribution.

is also smaller than that determined by the uncertainty analysis described in S5.) These results suggest that our region choice criteria have not biased our estimation of α_{eq}.

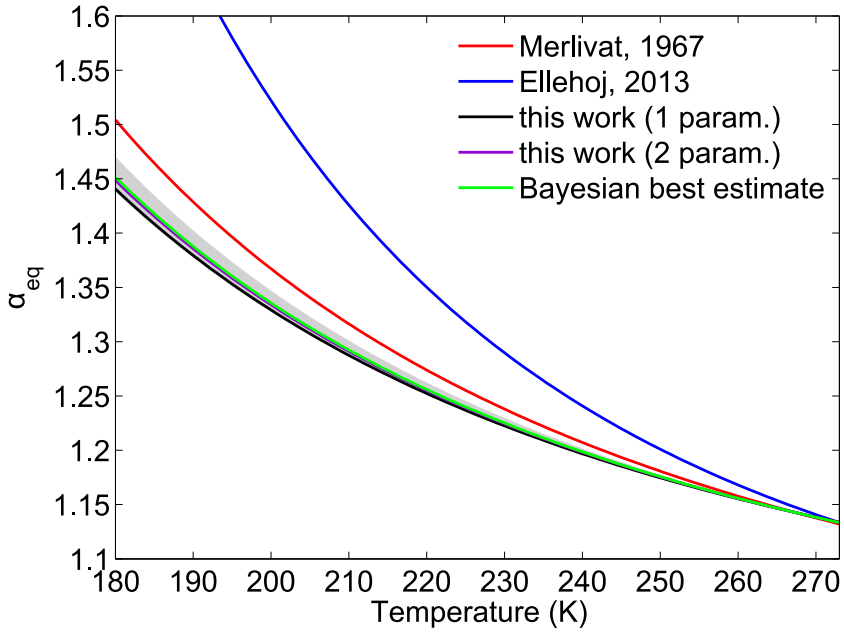

Figure S11: Test of sensitivity of global fit to region choice for individual experiments. We randomly vary parameters that determine the experiment region, then calculate the best global fit as described in the text (using a 2-parameter fit). The expectation value of the resulting probability distribution is shown in green. Gray shaded region is the 99.73% confidence interval derived from the probability distribution. Results suggest that our region choice has not introduced systematic bias. The Bayesian best estimate gives $a_0 = -0.0649$ and $a_1 = 14171$, which is very close to the best 2-parameter fit with the region choice used in the analysis. (In this test we take d from Merlivat, 1978, but d negligibly affects results; see S7.2 below.)

Bayesian analysis methods: The estimator of a_1 computed in Eq. (18) implicitly depends on the chosen values of ϵ, Γ, and Δ and can be seen as deterministic when these parameters are fixed. In this analysis we treat $\hat{a}_1$ as a random variable with a PDF related to probability distributions of ϵ, Γ, and Δ:

$$\begin{aligned} p\left(\hat{a}_1\right) &= \iiint_{-\infty}^{+\infty} p\left(\hat{a}_1 | \epsilon, \Gamma, \Delta\right) p\left(\epsilon, \Gamma, \Delta\right)\, d\epsilon\, d\Gamma\, d\Delta \\ &= \iiint_{-\infty}^{+\infty} \boldsymbol{\delta}\left(\hat{a}_1 - \hat{a}_1\left(\epsilon, \Gamma, \Delta\right)\right) p\left(\epsilon, \Gamma, \Delta\right)\, d\epsilon\, d\Gamma\, d\Delta \end{aligned} \tag{26}$$

where $\boldsymbol{\delta}$ represents the Dirac distribution. If ϵ, Γ, and Δ are independent and uniformly distributed between bounds, we can draw n samples (with n sufficiently large; we use $n = 100$) and evaluate the density of $\hat{a}_1$ as:

$$p\left(\hat{a}_1\right) \approx \frac{1}{n} \sum_{k=1}^{n} \boldsymbol{\delta}\left(\hat{a}_1 - \hat{a}_1\left(\epsilon_k, \Gamma_k, \Delta_k\right)\right) \tag{27}$$

or, more conveniently, to give a continuous representation of the density:

$$p\left(\hat{a}_1\right) \approx \frac{1}{n}\sum_{k=1}^{n} \mathbf{G}\left(\hat{a}_1 - \hat{a}_1\left(\epsilon_k, \Gamma_k, \Delta_k\right)\right) \tag{28}$$

where $\mathbf{G}$ is a Gaussian kernel of suitable width. The most probable $\hat{a}_1$ and confidence intervals on the estimate can then be computed from the probability distribution $p\left(\hat{a}_1\right)$.

S7.2 Sensitivity to estimation of kinetic isotope effects

In this section we test the robustness of our estimation of α_{eq} to uncertainties that affect the calculated kinetic modification to fractionation: uncertainty in the isotopic diffusivity ratio d and potential systematic bias in the measurement of H_2O. Resulting errors in calculated kinetic effects could affect the global estimate of α_{eq}.

Isotopic diffusivity ratio (d)
In section S6, we showed that different assumed values of d could significantly alter the slope of inferred $\hat{\alpha}_n$ against supersaturation. Those changes have a much smaller effect on the global fit for α_{eq}, because the global fit of the IsoCloud 4 dataset is dominated by experiments with small supersaturations and minimal kinetic effects. Varying d over the range of published estimates (∼3% variation, see Table S5) can affect estimation of $\hat{\alpha}_n$ in individual experiments by as much as 1-2% (Figure S12), but has virtually no effect on the retrieval of α_{eq}, producing a maximum change of 0.02%. (We do not show a figure for this test because the differences in α_{eq} are too small to be visible by eye.) Uncertainty in d therefore cannot bias our estimate of α_{eq}.

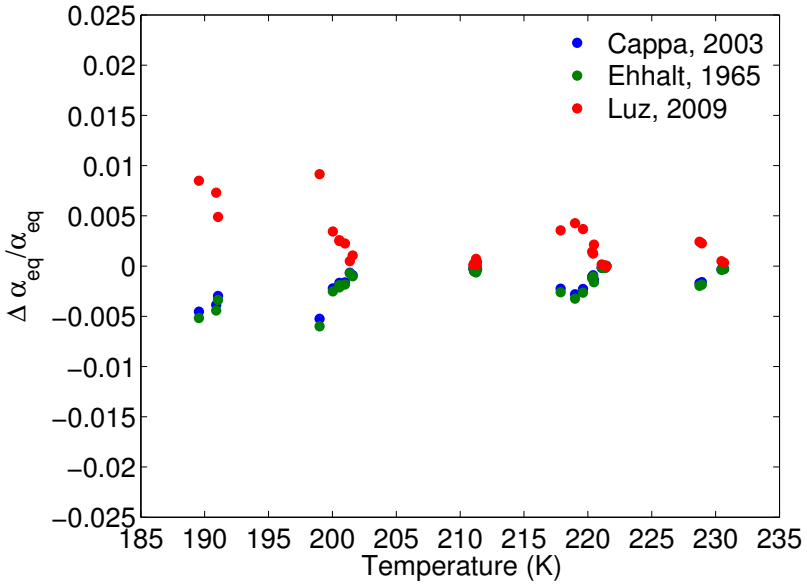

Figure S12: Effect of choices for the isotopic diffusivity ratio d on inferred $\hat{\alpha}_n$ for individual experiments. We use the value of d from Merlivat 1978 as the reference and show differences when d is taken instead from Cappa et al. 2003 (blue), Ehhalt and Knott 1965 (green), and Luz et al. 2009 (red). Individual experiments may be affected by up to 1-2% , but the global fit for the temperature dependence of α_{eq} must intersect the cluster of near-equilibrium experiments at ∼210 K that show negligible dependence on d.

Supersaturation

Systematic bias in H_2O measurements can affect estimates of isotopic fractionation in several ways: by changing the inferred ice deposition rate, and by producing a biased measurement of supersaturation S_i and so a biased calculation of the kinetic modification to fractionation. The latter effect is by far the most important. Systematic measurement bias is common for measurements of gas-phase species by absorption spectroscopy that do not involve empirical calibration, since spectral line parameters are not perfectly known. For the ChiWIS H_2O measurements, stated uncertainties on line parameters from the HITRAN database [14, 15] nominally limit the water vapour retrieval to an accuracy of $\pm 5\%$. However, ChiWIS measured vapour pressure in dense ice clouds, when water vapour should be drawn down to saturation, suggests that ChiWIS H_2O measurements are accurate to within -1% and $+2\%$. (These limits are 2 standard deviations around the mean of calculated ChiWIS S_i, using [38] for saturation vapour pressure.) Potential biases of this magnitude would produce noticeable changes in estimated α_{eq}, since experiments at $S_i \sim 1$ would then be assumed to experience super- or sub-saturation and kinetic modifications to fractionation. The effect is shown in Fig. S13. Systematic over- or under-estimation of supersaturation is the largest source of systematic uncertainty in our analysis. However, the range of potential changes remains within the 3σ confidence interval of the best fit presented here.

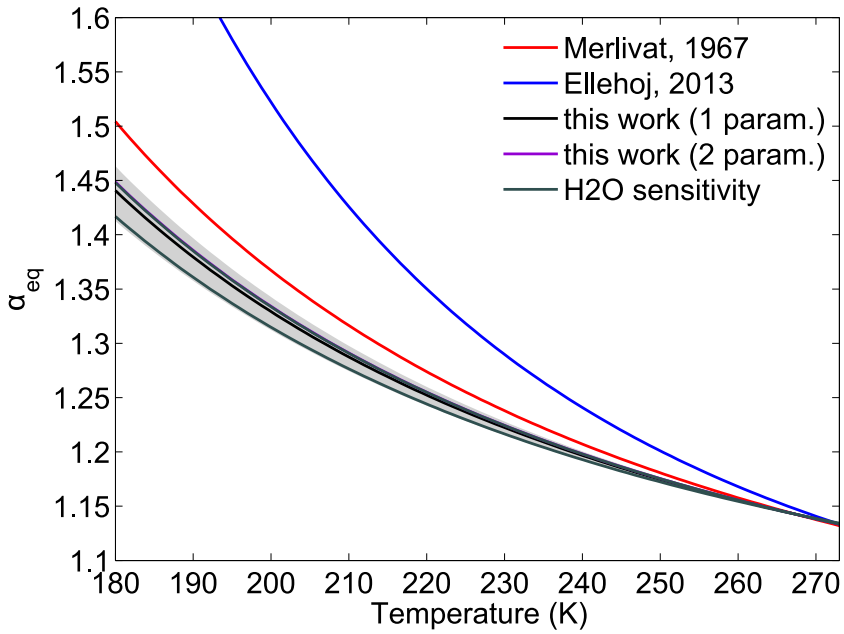

Figure S13: Sensitivity of fit for α_{eq} to potential fractional bias in water vapour and therefore S_i. Black line shows default best-fit α_{eq}; grey lines repeat analysis with assumption that ChiWIS H_2O has bias of $+2\%$ and -1%. Overestimating H_2O would lead to overestimating kinetic modification to fractionation and so α_{eq}; the true value of α_{eq} would then be lower than estimated. Similary, underestimating H_2O would mean the true value of α_{eq} would be higher than estimated. Gray shaded region is the 3σ confidence interval described previously.

S7.3 Sensitivity to weights on individual experiments

As mentioned previously, our estimated experimental uncertainties may be subject to temperature-dependent bias. The global fit procedure, which weights individual experiments by their estimated error, may therefore over-weight the warm-temperature experiments relative to those at $T < 210$ K. We test for any resulting bias in determination of α_{eq} by comparing to a fit with all experiments treated equally. The parametrizations for α_{eq} in the weighted and unweighted fits are not significantly different (Figure S14). (The parameters in the unweighted fit are a_0= -0.0595 and a_1=13837; compare to values in Table S4.) Our estimate of α_{eq} appears robust to errors in the weighting of individual experiments.

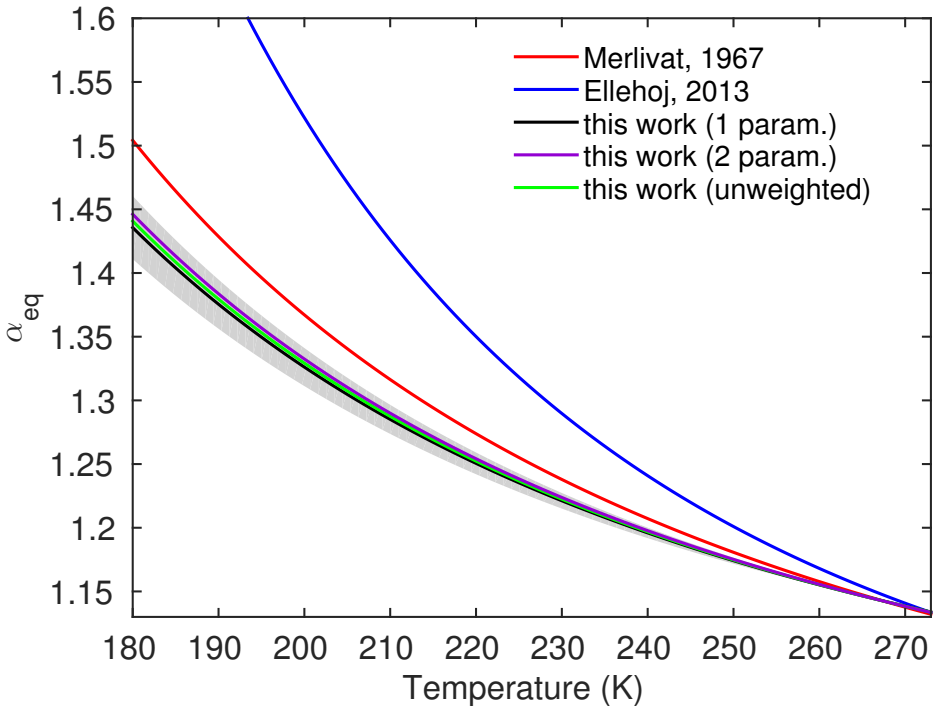

Figure S14: Sensitivity of the fit for α_{eq} to potential uncertainty in the weighting of individual experiments. Black line shows default best-fit α_{eq} using weights derived from the uncertainty analysis; green line repeats the analysis with equal weighting for all experiments. Gray shaded region is the 3σ confidence interval described previously.

References

[1] J. Bigeleisen. Statistical mechanics of isotopic systems with small quantum corrections. I. General considerations and the rule of the geometric mean. *The Journal of Chemical Physics*, 23(12):2264–2267, 1955.

[2] H. C. Urey. The thermodynamic properties of isotopic substances. *J. Chem. Soc.*, pages 562–581, 1947.

[3] S. Matsuo, H. Kuniyoshi, and Y. Miyake. Vapor pressure of ice containing D_2O. *Science*, 145(3639):1454–1455, 1964.

[4] L. Merlivat and G. Nief. Fractionnement isotopique lors des changements d'état solide-vapeur et liquide-vapeur de l'eau à des températures inférieures 0°C. *Tellus*, 19(1):122–127, 1967.

[5] W. A. Van Hook. Vapor pressures of the isotopic waters and ices. *The Journal of Physical Chemistry*, 72(4):1234–1244, 1968.

[6] M. Johansson and K. Holmberg. Separation of heavy water in phase equilibria involving pure water or salt-water systems. *Acta Chemica Scandinavica*, 23:765–781, 1969.

[7] J. D. Pupezin, G. Jakli, G. Jancso, and W. A. Van Hook. Vapor pressure isotope effect in aqueous systems. I. water-water-D2 (-64.deg. to 100.deg.) and water-water18-O (-17.deg. to 16.deg.). Ice and liquid. II. Alkali metal chloride solution in water and water-D2 (-5.deg. to 100.deg.). *The Journal of Physical Chemistry*, 76(5):743–762, 1972.

[8] M. Méheut, M. Lazzeri, E. Balan, and F. Mauri. Equilibrium isotopic fractionation in the kaolinite, quartz, water system: Prediction from first-principles density-functional theory. *Geochimica et Cosmochimica Acta*, 71(13):3170–3181, 2007.

[9] M. D. Ellehøj, H. C. Steen-Larsen, S. J. Johnsen, and M. B. Madsen. Ice-vapor equilibrium fractionation factor of hydrogen and oxygen isotopes: Experimental investigations and implications for stable water isotope studies. *Rapid Communications in Mass Spectrometry*, 27(19):2149–2158, 2013.

[10] C. Pinilla, M. Blanchard, E. Balan, G. Ferlat, R. Vuilleumier, and F. Mauri. Equilibrium fractionation of H and O isotopes in water from path integral molecular dynamics. *Gechemica et Cosmochimica Acta*, 135:203–216, 2014.

[11] O. Möhler, O. Stetzer, S. Schaefers, C. Linke, M. Schnaiter, R. Tiede, H. Saathoff, M. Krämer, A. Mangold, P. Budz, P. Zink, J. Schreiner, K. Mauersberger, W. Haag, B. Kärcher, and U. Schurath. Experimental investigation of homogeneous freezing of sulphuric acid particles in the aerosol chamber AIDA. *Atmos. Chem. Phys.*, 3:211–223, 2003.

[12] C. Lauer. *Aufbau und Validierung eines kalibrationsfreien, extraktiven 1.4 um-Laserhygrometers für den Einsatz an der Aerosolkammer* AIDA. PhD thesis, 2007.

[13] J. Skrotzki. *High-accuracy multiphase humidity measurements using TDLAS: application to the investigation of ice growth in simulated cirrus clouds*. PhD thesis, 2012.

[14] L. S. Rothman, D. Jacquemart, A. Barbe, D. C. Benner, M. Birk, L. R. Brown, M. R. Carleer, C. Chackerian, K. Chance, and L. H. et al. Coudert. The HITRAN 2004 molecular spectroscopic database. *Journal of Quantitative Spectroscopy and Radiative Transfer*, 96(2):139–204, 2005.

[15] L. S. Rothman, I. E. Gordon, A. Barbe, D. C. Benner, P. F. Bernath, M. Birk, V. Boudon, L. R. Brown, A. Campargue, and J.P. et al. Champion. The HITRAN 2008 molecular spectroscopic database. *Journal of Quantitative Spectroscopy and Radiative Transfer*, 110(9):533–572, 2009.

[16] R. Wagner and O. Möhler. Heterogeneous ice nucleation ability of crystalline sodium chloride dihydrate particles. *Journal of Geophysical Research: Atmospheres*, 118(10):4610–4622, 2013.

[17] O. Möhler, P. R. Field, P. Connolly, S. Benz, H. Saathoff, M. Schnaiter, R. Wagner, R. Cotton, M. Krämer, A. Mangold, and A. J. Heymsfield. Efficiency of the deposition of mode ice nucleation on mineral dust particles. *Atmos. Chem. Phys.*, 6:3007–3021, 2006.

[18] J. U. White. Long optical paths of large aperture. *J. Opt. Soc. Am.*, 32(5):285–285, May 1942.

[19] J. U. White. Very long optical paths in air. *JOSA*, 66(5):411–416, 1976.

[20] L. Sarkozy, B. Clouser, K. Lamb, E. Stutz, H. Saathoff, V. Ebert, S. Wagner, B. Kühnreich, and E. Moyer. TDL spectrometer for chamber-based isotopic measurements of water vapor isotopic evolution during cirrus formation. *submitted to Review of Scientific Instruments*, 2017.

[21] H. Craig. Isotopic variations in meteoric waters. *Science*, 133(3465):1702–1703, 1961.

[22] R. Hagemann, G. Nief, and E. Roth. Absolute isotopic scale for deuterium analysis of natural waters. Absolute D/H ratio for SMOW1. *Tellus*, 22(6):712–715, 1970.

[23] P. Baertschi. Absolute ^{18}O content of standard mean ocean water. *Earth and Planetary Science Letters*, 31(3):341–344, 1976.

[24] R. J. Cotton, S. Benz, P.R. Field, O. Möhler, and M. Schnaiter. Technical note: A numerical test-bed for detailed ice nucleation studies in the AIDA cloud simulation chamber. *Atmos. Chem. Phys.*, 7:243–256, 2007.

[25] J. Jouzel and L. Merlivat. Deuterium and oxygen 18 in precipitation: Modeling of the isotopic effects during snow formation. *Journal of Geophysical Research*, 89:11749–11757, 1984.

[26] J. Nelson. Theory of isotopic fractionation on facetted ice crystals. *Atmospheric Chemistry and Physics*, 11(22):11351–11360, 2011.

[27] M. Bolot, B. Legras, and E. J. Moyer. Modelling and interpreting the isotopic composition of water vapour in convective updrafts. *Atmos. Chem. Phys.*, 13(16):7903–7935, 2013.

[28] D. A. Fisher. Remarks on the deuterium excess in precipitation in cold regions. *Tellus B*, 43:401–407, 1991.

[29] M. Ghil, M. R. Allen, M. D. Dettinger, K. Ide, D. Kondrashov, M. E. Mann, A. W. Robertson, A. Saunders, Y. Tian, F. Varadi, and P. Yiou. Advanced spectral methods for climatic time series. *Reviews of Geophysics*, 40(1):3–1–3–41, 2002.

[30] J. Bigeleisen. Statistical Mechanics of Isotope Effects on the Thermodynamic Properties of Condensed Systems. *The Journal of Chemical Physics*, 34(5):1485–1493, 1961.

[31] R. E. Criss. Temperature dependence of isotopic fractionation factors. *Stable Isotope Geochemistry: A Tribute to Samuel Epstein*, 3:11–16, 1991.

[32] J. Skrotzki, P. Connolly, M. Schaniter, H. Saathoff, O. Möhler, R. Wagner, M. Niemand, V. Ebert, and T. Leisner. The accommodation coefficent of water molecules on ice-cirrus cloud studies at the AIDA simulation chamber. *Atmos. Chem. Phys.*, 12:24351–24393, 2012.

[33] W. D. Hall and H. R. Pruppacher. The survival of ice particles falling from cirrus clouds in subsaturated air. *Journal of the Atmospheric Sciences*, 33(10):1995–2006, 1976.

[34] C. D. Cappa, M. B. Hendricks, D. J. DePaolo, and R. C. Cohen. Isotopic fractionation of water during evaporation. *Journal of Geophysical Research: Atmospheres*, 108(D16), 2003.

[35] D. Von Ehhalt and K. Knott. Kinetische Isotopentrennung bei der Verdampfung von Wasser. *Tellus*, 17(3):389–397, 1965.

[36] L. Merlivat. Molecular diffusivities of $H_2^{16}O$, $HD^{16}O$, and $H_2^{18}O$ in gases. *The Journal of Chemical Physics*, 69(6):2864–2871, 1978.

[37] B. Luz, E. Barkan, R. Yam, and A. Shemesh. Fractionation of oxygen and hydrogen isotopes in evaporating water. *Geochimica et Cosmochimica Acta*, 73(22):6697–6703, 2009.

[38] D. M. Murphy and T. Koop. Review of the vapour pressures of ice and supercooled water for atmospheric applications. *Quarterly Journal of the Royal Meteorological Society*, 131(608):1539–1565, 2005.